Acta Materialia 281 (2024) 120392

Contents lists available at ScienceDirect

Acta Materialia

journal homepage: www.elsevier.com/locate/actamat

A coupled model for precipitation strengthening in Mg-Zn alloys

Yi Yang [a,*], Jun Wang [a], Mahmoud Reza Ghandehari Ferdowsi [a], Sitarama R. Kada [a], Thomas Dorin [a], Matthew R. Barnett [a], Michel Perez [b,*]

[a] *Institute for Frontier Materials, Deakin University, Geelong, VIC 3216, Australia*
[b] *Université de Lyon, INSA-Lyon, MATEIS UMR CNRS 5510, 69621 Villeurbanne, France*

ARTICLE INFO

Keywords:
Magnesium alloy
Aging
Precipitation kinetics
Precipitation strengthening
Modeling

ABSTRACT

A recently developed precipitation model is coupled to an original mechanical model to predict the strength evolution in Mg-Zn alloys during aging. The proposed models consider the strengthening effects of rod and plate-shaped precipitates on the most important deformation mechanisms in Mg alloys: basal slip, prismatic slip, and twinning. It is found that shearing of rod precipitates dominates the strengthening on basal slip at early aging stages, while the bypass mechanism dominates medium and over-aging stages. On prismatic planes, the bypass of rod precipitates dominates across all aging stages. The influence of different precipitate arrangements and aspect ratios on modelling results is also discussed. The strengthening from plate-shaped precipitates is found to be very poor for the studied slip modes. While for twinning, the strength evolution is nicely represented by bypassing of rod-shaped precipitates. The evolutions of tensile and compressive yield strength during aging are well predicted by considering the hardening on prismatic and twinning planes, respectively.

1. Introduction

Developing high strength magnesium (Mg) alloys is of great interest since it has the potential of "light weight" applications in aerospace, transportation and biomedical products due to its high specific strength and bio-degradable features [1-5]. Strengthening through age hardening, a typical approach in metallic alloys, involves the formation of nano-scale precipitates that hinder dislocation movement [6]. While the fundamental mechanisms governing the interaction between dislocations and precipitates are well understood, the exact contribution of these mechanisms to the strength evolution during aging remains unclear. This uncertainty is particularly significant for Mg alloys, where basal, prismatic slip and twinning are readily activated during deformation, a characteristic of their hexagonal close-packed (hcp) structure.

The Mg-Zn system is an ideal candidate for investigating precipitation strengthening in Mg alloys, as it provides excellent age-hardening response [7]. Two distinct strengthening phases are reported in Mg-Zn alloys [8-18]: the rod-shaped β_1' precipitates along the *c*-axis and the plate-shaped β_2' precipitates with their broad face parallel to the basal plane. In the precipitation sequence, the rod-shaped precipitates typically form first followed by the plate-shaped ones. Their precipitation kinetics have been thoroughly reported in previous studies [13,19,20]. To accurately describe the strength evolution in Mg-Zn alloys, it is crucial to understand the role of rod and plate-shaped precipitates on the slip and twinning mechanisms.

Numerous studies have investigated the precipitation hardening on different slip planes in Mg alloys based on the precipitate shapes. This is usually achieved by evaluating the critical resolved shear stress (CRSS) difference before and after aging. Initial investigations used single crystal studies [21] and have then progressed to poly-crystals using methods such as micropillars [12,22], nanoindentations [23] and in-situ diffraction [24-28]. For example, Wang et al. [12] suggested that the rod-shaped precipitates in an aged Mg-5 Zn alloy produce moderate increase of CRSS for basal slip of 17 MPa (33 %), based on micropillar compression results. Agnew et al. [29], using in-situ neutron diffraction and Elasto-Plastic Self-Consistent models (EPSC) modelling, found that prismatic plates in Mg alloys containing rare-earth elements increased the CRSS for basal slip from 12 MPa to 37 MPa, an increase of over 200 %, while the CRSS for prismatic slip increased by 18 %, from 78 MPa to 92 MPa. However, techniques like micropillars and indentation-based approaches are subject to size effects [12,22,23] and other artefacts that can lead to scattering results for the same system.

Regarding the equations that describe precipitation hardening, two types are normally considered [6,15,16,30,31]: (i) dislocation bypassing precipitates through the Orowan mechanism, and (ii) precipitate shearing. The Orowan equation, traditionally used for spherical

* Corresponding authors.
E-mail addresses: y.yang@research.deakin.edu.au (Y. Yang), michel.perez@insa-lyon.fr (M. Perez).

https://doi.org/10.1016/j.actamat.2024.120392
Received 2 April 2024; Received in revised form 9 September 2024; Accepted 9 September 2024
Available online 17 September 2024

particles, calculates the maximum stress required for a dislocation line to bow and bypass strong precipitates in a slip plane. In Mg alloys, with most precipitates having asymmetrical shapes, efforts have been made to modify the Orowan equation to account for precipitates with non-spherical shapes. Nie [16] and Robson et al. [15] applied a modified Orowan equation to calculate the hardening effect of precipitates with different geometries on basal and prismatic slips in Mg alloys. These studies have shown that the rod-shaped precipitates have stronger hardening effect on both slip systems compared to the plate-shaped precipitates. These predictions have been confirmed by recent Transmission Electron Microscopy (TEM) and in-situ diffraction studies [13, 25], and agree well with some other experimental CRSS estimations [11, 13,32]. However, these studies do not fully address the influence of different particle arrangements on the CRSS increments.

In Mg alloys, the precipitation hardening on slip is often well described by the Orowan equation, as bypassing is usually the dominant mechanism since most strengthening precipitates in Mg alloys are either too large or incoherent to be sheared [10]. Nonetheless, shearing has been observed in prior works, in thin prismatic plates and rod-shaped precipitates by basal slip as observed by TEM [33-36], though these findings are mostly based on single-crystal micropillar experiment where the shearing forces are significantly higher than in polycrystals. Bhattacharyya et al. [35] developed an order strengthening model predicting that the shearing resistance of precipitates may be related to the formation of anti-phase boundaries (APB) within the precipitates. The APB energy for basal slip was estimated to be 210 mJ/m^2, high enough to account for the observed shearing. While the shearing mechanism of precipitates in Mg alloys remains unclear, theoretical solutions for shearing have been proposed in some other systems such as aluminium (Al) alloys. Bardel et al. [37] introduced a coupled precipitation and strengthening model based on Orowan theories for a 6061 Al alloy, accounting for both shearing and bypassing mechanisms for needle-shaped precipitates.

Twinning also plays an important role in accommodating plastic deformation in Mg alloys, but evaluating precipitation hardening on twinning is complicated. Early studies [38-40] showed that precipitates can be sheared by $\{10\bar{1}2\}$ twins, particularly when precipitates are thin ($<$ 20 nm) and coherent with the matrix. However, twins do not usually shear precipitates [11,32,41]. Instead, the rod-shaped precipitates in Mg-Zn alloys tend to undergo a rigid body rotation of $\sim 4°$ as it interacts with a twin [11,15,38]. Gharghouri *et al.* [42] found that twins can either engulf, arrest at, or bypass precipitates depending on their size differences. The CRSS increment for twinning caused by precipitates has been evaluated in many studies through Visco-Plastic Self-Consistent (VPSC), micropillar compression and Schmid Factor method [11,15,32, 43,44]. In Mg alloys, the *c*-axis rods were found to increase CRSS for twinning by $\sim$ 30 – 60 MPa [11,44,45], while the basal plates caused an increase of $\sim$ 20 – 50 MPa [28,32,46]. These results vary depending on the methods used to determine the onset of twinning. The classical Orowan equation has also been applied to study precipitate strengthening against twinning [15,16], where the twin partial dislocation is treated in the same way as a lattice slip dislocation to bypass the precipitates. However, since the Burgers vector of twinning dislocations is much smaller than that of slip, the predicted hardening from the Orowan equation ($\sim$ 5 – 10 MPa) is lower than the CRSS values reported above ($\sim$ 20 – 60 MPa) [11,15,32,43,44]. Recently, Barnett et al. [47] proposed a double super dislocation model for the propagation of twins based on Orowan theory, where the movement of the twin tip can be seen as a set of twin partials, with the leading dislocation being “pushed” by a trailing super dislocation to bypass the particles. This model reasonably predicts the observed CRSS increment in a Mg-6 Zn alloy [44, 47].

Despite extensive reporting on precipitation hardening on slip and twinning in Mg-Zn alloys, few studies have attempted to couple strength models with precipitation kinetics models. Consequently, the strength evolution during aging in Mg-Zn alloys with rod-shaped precipitates has not been well described, and the relative importance of different strengthening mechanisms contributing to the strength evolution have not been thoroughly discussed.

This study aims at investigating the precipitation hardening mechanism on basal, prismatic slips and twinning in Mg-Zn alloys following precipitation kinetics, and eventually the yield strength evolution during aging, through strengthening models coupled with a precipitation kinetics model. The precipitation modelling strategy and microstructural information will be referenced from a recent paper [20] where the precipitation kinetics in the same Mg-Zn alloy is characterized and modelled in detail through multiple characterization techniques and a precipitation model. The strengthening model for slip is built on the classical theories that depict interactions between dislocations and particles, and the model for twinning is based on the super dislocation model proposed by Barnett et al. [47]. All strengthening models are modified to consider poly-dispersed precipitates calculated from precipitation kinetics model. Finally, the modelling results are compared with experimental data and the hardening mechanisms of precipitates on different deformation modes are discussed.

2. Methodology

2.1. Material and heat treatment

The material and heat treatment conditions used in this study are following [20]. Briefly, extruded Mg - 4.5wt% Zn alloy as the example material to validate the model. This composition was selected for its considerable precipitate volume fraction after heat treatment while avoiding unstable solid solution and Zn clustering [48]. The production of this material starts from the solution treatment under Argon gas atmosphere of cast Mg - 4.5wt% Zn alloy at 330 °C for 24 h and 370 °C for 120 h, followed by extrusion at 350 °C with a reduction ratio of $\sim$ 36 and a ram speed of 0.1 mm/s. The obtained microstructure has a grain size of $\sim$ 20 μm. The extruded samples are then artificially aged at 150 °C and 200 °C for up to 180 h in an air furnace, followed by quenching in water at room temperature. Note that the effect from oxidization is excluded, as all samples were sealed within stainless steel foil when aging, and the aging temperatures (150 and 200 °C) were significantly lower than the critical temperature reported for aggressive oxidization to occur ($\sim$400 °C) [49].

2.2. Tensile and compression tests

The compression and tensile samples are cut from the centre of the extruded and aged material. The cylindrical compression samples have a height of 6 mm and a diameter of 4 mm. The tensile tests used miniatured samples, the gauge size of which is presented in Fig. 1. Three samples were tested for each condition. Compression and tensile tests were carried out using a universal INSTRON machine, with a compression strain rate of 2×10^{-4} s^{-1} and a tension strain rate of 1×10^{-3} s^{-1}, in a direction parallel to the extrusion direction (ED) so that the $\{10\bar{1}2\}$ twinning dominates the compression stress-strain behaviour and prismatic slip dominates in tension.

2.3. Precipitation kinetics model

The precipitation kinetics model used in this study is built on classical nucleation and coarsening theories where nucleation, growth and coarsening are calculated at a continuous level. The principal equations were adapted for rod and plate-shaped precipitates in the PreciSo software which are fully described in [20].

This model is based on several assumptions:

- The nucleation is homogeneous.

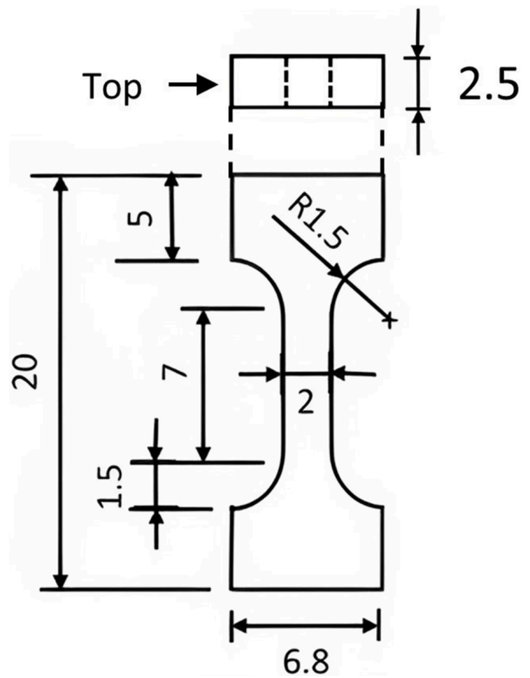

Fig. 1. Schematic illustration of a tensile sample used for the study (units are in mm).

- The interfacial energy of precipitates decreases with increasing temperature and does not change with precipitate size and other aging conditions.
- The chemical composition and aspect ratio of precipitates does not vary with precipitate size and aging conditions.
- The solute diffusion rate does not vary with crystal orientations.

For nucleation, the total Gibbs energy change ΔG with the presence of precipitates can be expressed as follows:

Rods [37]:

$$\Delta G = \left(b_r - \frac{2}{3}\right)\pi r_r^3 \Delta g + b_r 2\pi r_r^2 \gamma \tag{1}$$

Plates [50]:

$$\Delta G = \frac{2}{b_p}\pi r_p^3 \Delta g + \left(1 + \frac{2}{b_p}\right) 2\pi r_p^2 \gamma \tag{2}$$

Where Δg is the chemical driving force (negative) and γ is the surface energy, r_r is the radius of rod-shaped precipitates, b_r is the shape factor (length over radius) of rod-shaped precipitates, r_p is the radius of plate-shaped precipitates, b_p is the shape factor (diameter over thickness) of plate-shaped precipitates.

The energy barriers for nucleation are:

Rods [37]:

$$\Delta G^* = \frac{16}{3}\pi \frac{\gamma^3}{\Delta g^2} \frac{2b_r^3}{(3b_r - 2)^2} \tag{3}$$

Plates [50]:

$$\Delta G^* = \frac{16}{3}\pi \frac{\gamma^3}{\Delta g^2} \frac{(b_p + 2)^3}{18 b_p} \tag{4}$$

The classical nucleation rate for rod and plate-shaped precipitates is given by [51]:

$$\frac{dN}{dt} = N_0 Z \beta^* \exp\left[-\frac{\Delta G^*}{k_b T}\right]\left[1 - \exp\left(-\frac{t}{\tau}\right)\right] \tag{5}$$

Where t is the aging time, τ is the incubation time, T is the temperature, k_b is the Boltzmann constant, N_0 is the nucleation site density, the current study considers homogeneous nucleation where every atom of the matrix is a possible nucleation site, then $N_0 = \frac{1}{v_{at}^m}$, where v_{at}^m is the atomic volume of the matrix. β^* is the condensation rate and Z is the Zeldovich factor.

For growth and coarsening, modified Zener-Hillert expressions are used:

Rods [37]:

$$\frac{dl}{dt} = 1.5\frac{D_{Zn}}{2r_r}\frac{X_{Zn} - X_{Zn}^i}{\alpha X_{Zn}^p - X_{Zn}^i} \tag{6}$$

Plates [50]:

$$\frac{dl}{dt} = 0.5 b_p \frac{D_{Zn}}{r_p}\frac{X_{Zn} - X_{Zn}^i}{\alpha X_{Zn}^p - X_{Zn}^i} \tag{7}$$

Where D_{Zn} is the Zn diffusion coefficient, α is the ratio of atomic volume between matrix and precipitate, X_{Zn} is Zn atomic fraction in the matrix, X_{Zn}^p is the Zn atomic fraction in the precipitate, X_{Zn}^i is Zn atomic fraction at the interface.

The precipitate size evolution in this model is described with a "mean field multi-class approach" (Lagrangian-like approach) where, in a precipitate size class, the size of precipitates evolves with time but its proportion remains constant. The mass balance is calculated to update the solute content as precipitation proceeds using:

$$X_{Zn} = \frac{X_{Zn}^0 - \alpha X_{Zn}^p f_v}{1 - \alpha f_v} \tag{8}$$

Where f_v is the volume fraction of precipitates at each time step which can be calculated by knowing the radius and number density of precipitates from the model, X_{Zn}^0 is the initial atomic fraction of Zn in solid solution, here $X_{Zn}^0 = 0.0172$. Here we assume the β_1' precipitate composition is Mg_4Zn_7, corresponding $X_{Zn}^p = 7/11$, and β_2' precipitate composition is $MgZn_2$, corresponding $X_{Zn}^p = 2/3$.

For more details of the precipitation model, readers are referred to [20]. It should be noted that the effects of solute clustering or GP zone are not considered in the current work as the previous study [20] shows no evidence of solute clustering (or GP zone) in the material extruded at the same condition, based on the Thermo-electric Power (TEP) analysis.

2.4. Precipitation strengthening model for slip

The strengthening model for slip used in this study is based on the classical formulations proposed by Friedel [52] and improved by Kocks [53] and Deschamps [54], with principles fully described in Appendix.

Where a dislocation line interacts with particles, the CRSS increment can be determined by the net force acting on the particles and the particle spacing [53,54], varying depending on whether the particle is sheared or bypassed.

For sheared particles, the CRSS increment is:

$$\Delta\tau^{sh} = \mu\sqrt{\frac{k^3 \bar{r}^3 N_a}{2\beta b}} \tag{9}$$

Where N_a is the area density of particles, b is the Burgers vector, β is the tension line constant, μ is the shear module, $\bar{r}$ is the average intersect radius of precipitates with the shear plane and k is a constant.

For bypassed particles, the CRSS increment is:

$$\Delta\tau^{bp} = \frac{2\beta\mu b}{L} \tag{10}$$

Where L is the particle spacing.

The $\bar{r}$, N_a and L adapted for rods and plates in different deformation modes will be presented in later sections.

The critical radius r_c where the shearing to bypassing transition occurs and the forces for shearing and bypassing are equal is defined as [37]:

$$r_c = \frac{2\beta b}{k} \tag{11}$$

2.5. Precipitation strengthening model for twinning

The mechanical model for twinning in this study is based on a double super dislocation model proposed by Barnett et al. [47]. In this model, the principal equation is:

$$\Delta\tau = \frac{\tau_0 G(n'b)^2}{2\pi\sqrt{1-\nu}2\gamma L_{twin}} \ln\left(\frac{\overline{D}}{n'b}\right) \tag{12}$$

Where τ_0 is the obstacle free reference propagation stress $\tau_0 = \frac{2\gamma}{nb}$, 2γ is the coherent twin interface energy, ν is Poisson's ratio, L_{twin} is the effective precipitate spacing on the twinning plane, $\overline{D}$ is the harmonic mean of precipitate length l and particle diameter d, which is given by $2/\left(l^{-1}+d^{-1}\right)$, and $n'b$ is the magnitude of the leading super dislocation Burgers vector.

The term $n'b$ can be eliminated with an empirical relationship from:

$$n'b = b_0'\left(\frac{d}{b}\right)^{\frac{1}{3}} \tag{13}$$

Where d is the diameter of precipitates, and b_0' is an empirical coefficient. For twinning $b = 0.049$ nm and $b_0' = 0.22$ nm.

3. Results of precipitation kinetics model for Mg-Zn alloys

3.1. Model parameters

The precipitation kinetics model presented by Yang *et al.* [20] is used to provide microstructural information for strength calculations in Mg-Zn alloys. The material under study is the Mg-4.5 wt.%Zn alloy and the parameters used are shown in Table 1. To clearly distinguish the two precipitate species, all rod-shaped β_1' precipitates are assumed to have a composition of Mg_4Zn_7, and plate-shaped β_2' precipitates are considered to have a composition of $MgZn_2$. A and B are parameters used to calculate the solubility product of precipitates ($\log_{10}K_S = -\frac{A}{T} + B$). Since β^* in Eq. (5) only allows one lattice parameter [20]; thus, for the Mg alloy, which typically has two lattice parameters, an equivalent lattice parameter a are used to describe the jumping frequency of atoms. This parameter can be calculated as follows. First, the volume of the hcp lattice unit is divided by the actual number of atoms in this unit to obtain the average atomic volume. Second, assuming atoms are homogeneously distributed in the matrix, an equivalent cubic structure is defined with the same atomic volume, and its lattice parameter a can be back-calculated from the unit volume. It should be noted that different surface energies are selected as fitted parameters for precipitates formed at 150 °C and 200 °C. Whilst previously reported surface energy values for Mg alloys were first used [55,56] ($\sim$ 0.02 to $\sim$ 0.4 J/m^2), the final values selected are the ones that provide the best agreement between simulation and experimental results reported in Yang *et al.* [20]. This approximation is acceptable as the major focus of this study is not to validate the precipitation kinetics model, but to provide the best input for the strengthening model.

Table 1
Parameters used for precipitation model.

Parameters	$\beta_1'(Mg_4Zn_7)$	β_2' $(MgZn_2)$	Reference
X_{Zn}^0 (at%)	1.72	1.72	[20]
X_{Zn}^p	7/11	2/3	
Aspect ratio	25 (b_r)	2.5 (b_p)	[20]
A (K)	3759	1095	[20]
B	−6.89	−2.06	
D_{Zn}^0 (m^2/s)	2.9×10^{-5}	2.9×10^{-5}	[57]
Q_{Zn} (kJ/mol)	118.6×10^3	118.6×10^3	[57]
γ at 150 °C (J/m^2)	0.043	0.0773	fitted
γ at 200 °C (J/m^2)	0.04	0.0743	fitted
v_{at}^p (m^3)	1.72×10^{-29}	1.62×10^{-29}	[58]
α	1.35	1.43	[58]
Equivalent lattice parameter a (Å)	2.85×10^{-10}	2.85×10^{-10}	[20]

3.2. Precipitate size information for strength calculations

The formation kinetics of rod (Mg_4Zn_7) and plate-shaped ($MgZn_2$) precipitates in Mg-Zn alloys aged at 150 °C and 200 °C are calculated using the precipitation model. The simulations are validated against experimental results from several characterization techniques as reported in ref. [20]. Fig. 2 shows the simulated evolutions of precipitates' radius, number density and volume fraction. At early aging stage, the rod-shaped β_1' phase has a lower radius and higher number density compared to the plate-shaped β_2' phase (Fig. 1(a)-(d)). The rod-shaped β_1' phase dominates the precipitation process and reaches its maximum volume fraction when aged at 150 °C for $\sim$ 84 h or 200 °C for $\sim$ 12 h (Fig. 1(e) and (f)). Subsequently, the rod-shaped phase is gradually replaced by the plate-shaped β_2' phase. Overall, the simulated results align closely with the experimental data reported in [20]. The precipitate size distribution at each time step is also calculated to aid the strength calculation, some example conditions are shown in Fig. 3. These results are coupled with the strengthening model to calculate the strength evolution in the following sections.

4. Precipitation strengthening model for Mg-Zn alloys

4.1. Geometry relationship between precipitates and deformation planes

In this study, the mechanical model incorporates both the Orowan bypassing and the shearing mechanisms with a critical radius r_c where the dominating mechanism transitions from shearing to bypassing. For the shearing mechanism in Eq. (9), the particle spacing L was removed to emphasize the area density N_a rather than the particle arrangement. Contrastingly, for the bypassing mechanism in Eqs. (10) and (12), the crucial factor is the mean particle spacing on the slip and twinning planes. In Mg-Zn alloys, the two major strengthening precipitates are rod-shaped β_1' phase and plate-shaped β_2' phase. Their geometrical relationships with the basal, prismatic and twinning planes are depicted in Fig. 4. Rod precipitates align perpendicular to the basal plane and parallel to the prismatic plane. Plate precipitates have their large surface plane parallel to the basal plane and perpendicular to the prismatic plane. Both rods and plates intersect twinning plane at an angle.

4.2. Influence of precipitate arrangement

In the literature, two kinds of arrangements are proposed for this system: square (Robson *et al.* [15]) and triangular (Jain *et al.* [13] and Rosalie *et al.* [59]). To compare their influence on the strength calculation, mono-dispersed precipitates on slip planes are considered, where all precipitates are assumed to have the same size and are distributed homogeneously on each slip plane. This simple description of precipitate distributions will be expanded upon in later sections.

On the basal plane, both rod and plate precipitates have circular shape intersections. For homogeneously distributed rods with volume fraction f_v, length l and radius r, the particle spacing can be expressed as:

$$\text{For triangular arrangement}: \ L = r\sqrt{\frac{2\pi}{\sqrt{3}f_v}} - 2r \tag{14}$$

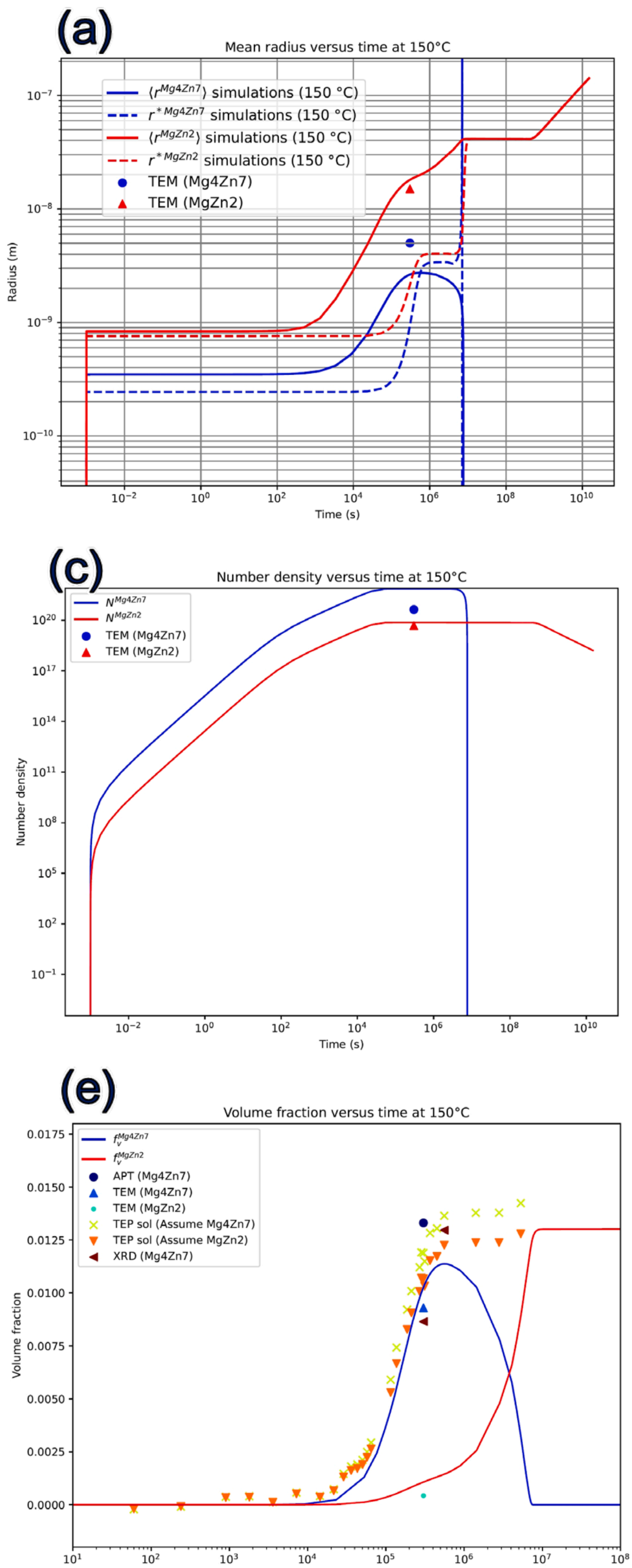

Fig. 2. Simulated radius, number density and volume fraction of rod (Mg_4Zn_7) and plate-shaped ($MgZn_2$) precipitates in Mg-Zn alloys aged at 150 °C and 200 °C. Results are compared with experiment data from Yang *et al.* [20], where "TEP-sol" means the precipitate volume fraction translated from the Themo-electric power measurement for solution treated samples.

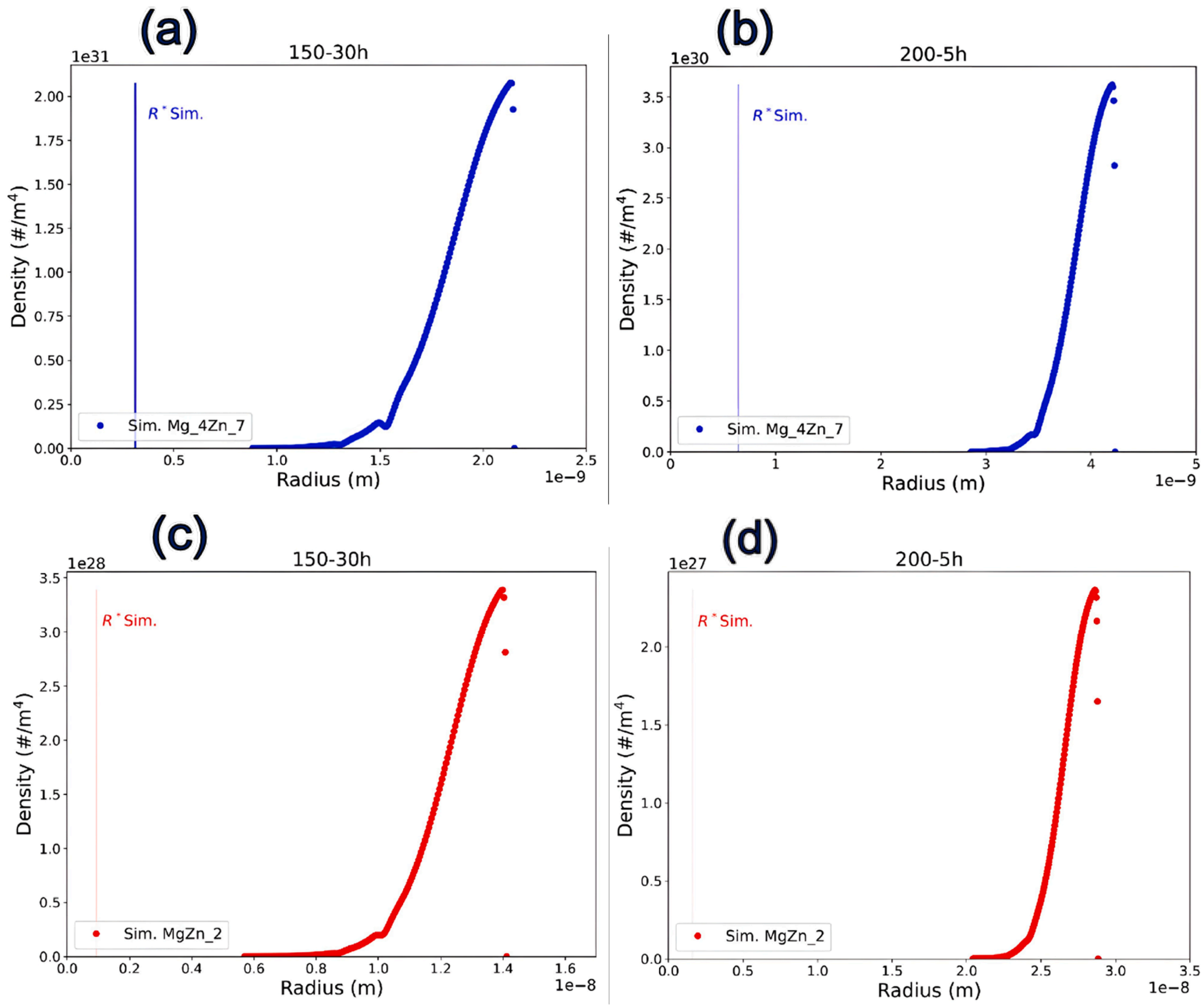

Fig. 3. Simulated precipitate size distributions of rod-shaped β_1' (Mg_4Zn_7) precipitates aged at (a)150 °C for 30 h and (b)200 °C for 5 h, and plate-shaped β_2' ($MgZn_2$) precipitates aged at (c)150 °C for 30 h and (d)200 °C for 5 h, in Mg-Zn alloys. All selected conditions are in the growth stage of precipitation. R^* is the critical radius for the precipitate to grow.

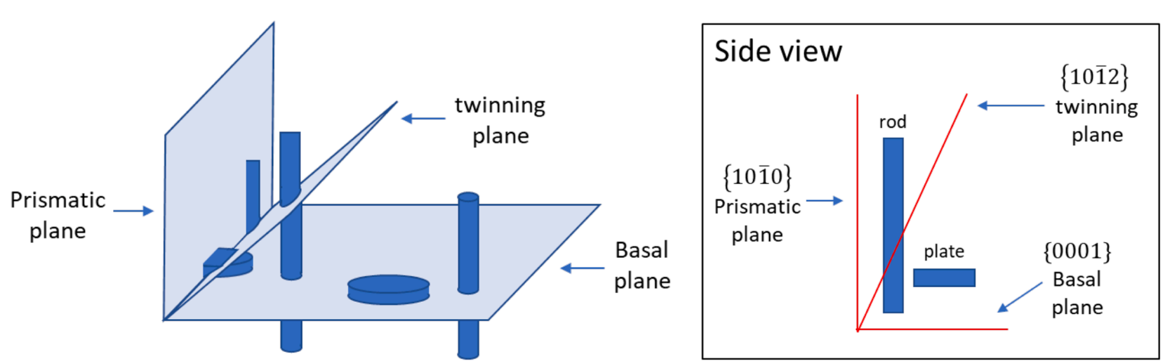

Fig. 4. intersection of rods and plates with basal, prismatic and twinning planes.

$$\text{For square arrangement}: \ L = r\sqrt{\frac{\pi}{f_v}} - 2r \tag{15}$$

Given their similar intersection shapes and geometrical relationships with the basal plane, rod and plate shaped precipitates follow the same expression for particle spacing. Comparing Eqs. (14) and (15), the difference between particle spacings for triangular and square arrangements is equal to $\sqrt{\frac{2}{\sqrt{3}}}$, which is close to 1, indicating a minor influence of particle arrangement on strengthening calculations.

On the prismatic plane, the intersections of rods have a near rectangular shape perpendicular to the basal plane. Their possible distributions are shown in Fig. 5. As seen, both arrangements have multiple sets of particle spacing values. Since the precipitation hardening is dominated by the smaller particle spacings, the effective particle spacing for square and triangular arrangements are L_{min} and L^*, respectively.

Considering a rod with length l and radius r intercepting a prismatic plane, the effective radius varies depending on the position of the precipitate relative to the intersecting plane, as shown in Fig. 6. The mean intersect radius $\bar{r}$ is related to r by:

$$\bar{r} = \frac{1}{r}\int_0^r \sqrt{r^2 - x^2}dx = r\frac{\pi}{4} \tag{16}$$

The effective particle spacing for a square arrangement is:

$$L_{min} = \sqrt{\frac{\pi r l}{2f_v}} - l \tag{17}$$

And for a triangular arrangement, the effective particle spacing is:

$$L^* = \sqrt{\left(L\frac{\sqrt{3}}{2} - l\right)^2 + \left(L\frac{1}{2} - 2\bar{r}\right)^2} \tag{18}$$

When the precipitates are plate-shaped, the intersection of precipitates on a prismatic plane remains rectangular with an arrangement similar to Fig. 5 but rotated 90°.

On the twinning plane, the intersection of rods can be approximated as circular areas similar to their projections on a basal plane. Thus, the distribution of rods on the twinning plane is similar to that on the basal plane, as depicted on Fig. 4, with a minor influence from different particle arrangements. The intersection of plates on the twinning plane resemble their projections on the prismatic plane with a near rectangle shape similar to Fig. 5 with a 90° rotation. Due to the asymmetrical nature of the precipitate intersections on the prismatic plane (Fig. 5), different precipitate arrangements could have significant impacts on the results.

Fig. 7 compares the influence of the two arrangements proposed in Fig. 5 on the particle spacing calculation, for the Mg-4.5 Zn alloy aged at 200 °C for 12 h as an example. The radius of rod-shaped precipitates is fixed at 5 nm and the number density of precipitates is fixed at 1.3 × 10^{20} m^{-3} (Table 2 in ref. [20]). The study investigates the smallest spacing in each arrangement relative to particle length, with all values normalized by the center-to-center distance L to emphasize the relative impact of particle shape and positioning.

From Fig. 7, it seems that triangular and square arrangements give close evaluations of particle spacing for short to medium rod lengths.

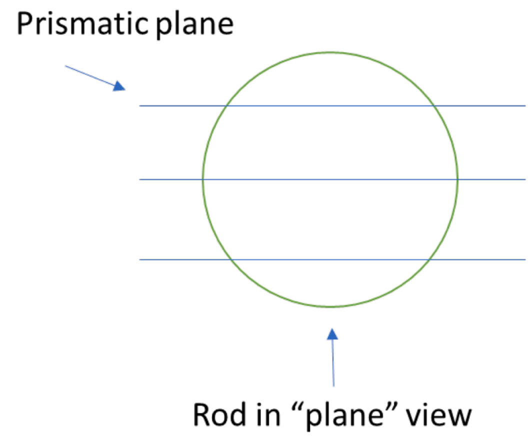

Fig. 6. Bottom view of rod intersection on prismatic plane. The effective radius varies depending on the position of the precipitate relative to the intersecting plane.

While for longer rods, both arrangements will meet their theoretical limit:

(a) For square arrangement, it tends to underestimate the particle spacing when rod is long. And the particle will overlap (where particle spacing goes to 0 and below) when the rod length equals to the particle center-to-center distance which can be expressed as $\sqrt{\frac{\pi r l}{2f_v}}$. When the precipitate is plate-shaped, this limit can be expressed as $\sqrt{\frac{\pi r t_p}{2f_v}}$, where t_p is the thickness of plate.

(b) For triangular arrangement, it provides a more stable configuration overall. But when the rod length gets close to the height of triangle, the smallest particle spacing L^* gradually lose its sensitivity to the particle shape and is eventually saturated as the rod side-to-side distance $L_{sat} = \frac{1}{2}L$, which does not vary with further particle shape change. The particle spacing could therefore be overestimated when the rod length is around this limit.

The upper limit of this saturation can be determined as $\frac{\sqrt{3}}{2}L = \frac{1}{2}\sqrt{\frac{\sqrt{3}\pi r l}{f_v}}$ for rod-shaped precipitates. When $l < \frac{1}{2}\sqrt{\frac{\sqrt{3}\pi r l}{f_v}}$, the smallest spacing L^* is well described by Eq. (18). When $l \geq \frac{1}{2}\sqrt{\frac{\sqrt{3}\pi r l}{f_v}}$, the smallest spacing becomes:

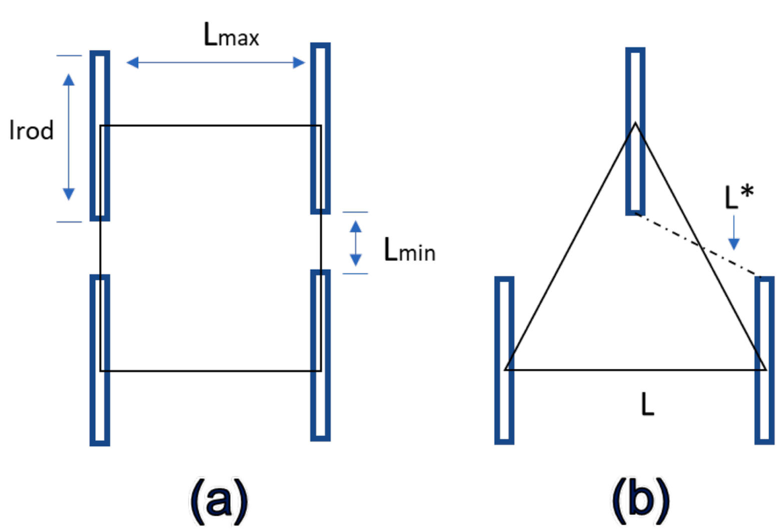

Fig. 5. Square and triangular arrangements of rod precipitate intersections on prismatic plane.

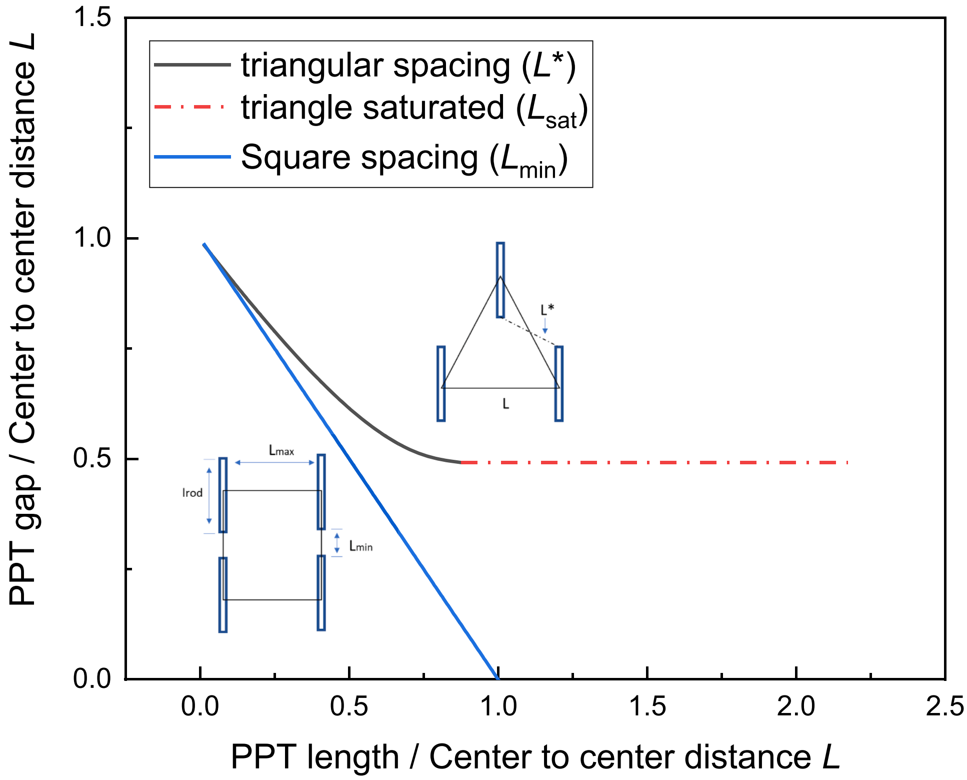

Fig. 7. The ratio between precipitate gap (PPT gap) and center-to-center spacing (*L*) vs The ratio between precipitate length (PPT length) and center-to-center spacing (*L*) for rod precipitates on prismatic plane. The triangular and square arrangements give close evaluations of particle spacing for short to medium rod lengths. While for longer rods, the difference becomes bigger and both arrangements will meet their theoretical limit.

$$L_{sat} = \frac{1}{2}L = \frac{1}{2}\sqrt{\frac{\pi rl}{\sqrt{3}f_v}} \tag{19}$$

When the precipitates are plate-shaped with a long side $\bar{r}$ and short side t_p, the upper limit for $\bar{r} = \frac{\pi r}{4}$ becomes $\frac{1}{2}\sqrt{\frac{\sqrt{3}\pi rt_p}{f_v}}$. When $r < 2\sqrt{\frac{\sqrt{3}rt_p}{\pi f_v}}$, smallest spacing L^* is:

$$L^* = \sqrt{\left(L\frac{\sqrt{3}}{2} - 2\bar{r}\right)^2 + \left(L\frac{1}{2} - t\right)^2} \tag{20}$$

When $r \geq 2\sqrt{\frac{\sqrt{3}rt_p}{\pi f_v}}$, the saturated smallest spacing becomes:

$$L_{sat} = \frac{1}{2}\sqrt{\frac{\pi rt_p}{\sqrt{3}f_v}} \tag{21}$$

4.3. *Model for poly-dispersed precipitates on slip planes*

To capture the full-strength evolution during aging, mechanical models are extended to poly-dispersed precipitates incorporating precipitate size distributions provided by the precipitation model.

4.3.1. *On* {0001} *basal plane*

As changing precipitate arrangement does not give much influence on strengthening prediction of basal plane, only triangularly arrangement is considered. The area density of precipitates intersecting the shear plane is the sum of all size classes in the precipitation model:

$$N_a = \frac{2}{\sqrt{3}L^2} = \sum_i N_{ai} = \sum_i N_i l_i' \tag{22}$$

Where N_{ai}, N_i and l_i' are the area density, number density and probability of intersection in size class *i*.

This leads to the estimation of the average precipitate center-to-center spacing:

$$L = \sqrt{\frac{2}{\sqrt{3}\sum_i N_i l_i}} \tag{23}$$

Where l_i is the precipitate length in size class *i*.

Assuming precipitates larger than r_c are bypassed and smaller ones are sheared, the CRSS increments due to bypassing and shearing are derived using Eqs. (9) and (10):

$$\Delta\tau_{bp} = \frac{2\beta\mu b}{\sqrt{\frac{2}{\sqrt{3}\sum_i N_i l_i}} - 2\frac{\sum_{i>i_c} N_i r_i}{\sum_{i>i_c} N_i}} \tag{24}$$

$$\Delta\tau_{sh} = \mu\sqrt{\frac{k^3\sum_{i<i_c} N_i l_i}{2b\beta}}\left(\frac{\sum_{i<i_c} N_i r_i}{\sum_{i<i_c} N_i}\right)^{\frac{3}{2}} \tag{25}$$

The shape and distribution of plate precipitates on the basal plane are the same as rod precipitates. For poly-dispersed plates the rod length *l* can be simply replaced by the plate thickness t_p:

$$\Delta\tau_{bp} = \frac{2\beta\mu b}{\sqrt{\frac{2}{\sqrt{3}\sum_i N_i t_{pi}}} - 2\frac{\sum_{i>i_c} N_i r_i}{\sum_{i>i_c} N_i}} \tag{26}$$

$$\Delta\tau_{sh} = \mu\sqrt{\frac{k^3\sum_{i<i_c} N_i t_{pi}}{2b\beta}}\left(\frac{\sum_{i<i_c} N_i r_i}{\sum_{i<i_c} N_i}\right)^{\frac{3}{2}} \tag{27}$$

4.3.2. *On* $\{10\bar{1}0\}$ *prismatic plane*

On prismatic plane, both triangular and square arrangements are considered to evaluate their differences on strength prediction. For the evaluation of critical radius between shearing and bypassing, rod intersections on prismatic planes are assumed spherical with an effective intersect radius. The average intersection area is:

$$\overline{S} = 2\overline{r}l = 2r\frac{\pi}{4}l \tag{28}$$

And the effective intersect radius is:

$$\overline{r}^* = \sqrt{\frac{\overline{S}}{\pi}} = \sqrt{\frac{rl}{2}} \tag{29}$$

For poly-dispersed precipitates, Eq. (29) becomes:

$$\overline{r}_i^* = \sqrt{\frac{\sum_i N_i r_i l_i}{2\sum_i N_i}} \tag{30}$$

And the area density can be expressed as:

$$N_a = \sum_i N_i 2r_i \tag{31}$$

To calculate the shearing strengthening of asymmetrically shaped precipitates, the shearing mechanism proposed by Nie et al. [60] for plates and rods in aluminium alloys is adopted to modify Eq. (9). The values of array exponent and efficient surface energy in Nie's equations [60] are considered fixed in the current study and naturally incorporated into the constant k. For rod-shaped precipitates, the CRSS increment for shearing becomes:

$$\Delta\tau_{sh} = k^{3/2} \times b_r \sqrt{\frac{\pi \sum_{i<i_c} N_i l_i}{b\beta\mu}} \tag{32}$$

For bypassing of triangularly arranged precipitates, the center-to-center spacing is:

$$L = \sqrt{\frac{2}{\sqrt{3}\sum_i N_i 2r_i}} \tag{33}$$

Considering Fig. 7 in Section 4.2, the critical situation for the triangular distribution to be saturated is when the precipitate length is equal to the height of the triangle. For poly-dispersed precipitates, the height of the triangle can be expressed as $\frac{\sqrt{3}}{2}L = \sqrt{\frac{\sqrt{3}}{2\sum_i N_i 2r_i}}$. Therefore, the CRSS increment due to bypassing can be calculated using Eqs. (10), (18), (19) and (33):

When $\frac{\sum_{i>i_c} N_i l_i}{\sum_{i>i_c} N_i} < \sqrt{\frac{\sqrt{3}}{2\sum_i N_{i>i_c} 2r_i}}$:

$$\Delta\tau_{bp} = \frac{2\beta\mu b}{\sqrt{\left(\sqrt{\frac{\sqrt{3}}{2\sum_{i>i_c} N_i 2r_i}} - \frac{\sum_{i>i_c} N_i l_i}{\sum_{i>i_c} N_i}\right)^2 + \left(\sqrt{\frac{1}{2\sqrt{3}\sum_{i>i_c} N_i 2r_i}} - \frac{\pi}{2}\frac{\sum_{i>i_c} N_i r_i}{\sum_{i>i_c} N_i}\right)^2}} \tag{34}$$

When $\frac{\sum_{i>i_c} N_i l_i}{\sum_{i>i_c} N_i} \geq \sqrt{\frac{\sqrt{3}}{2\sum_{i>i_c} N_i 2r_i}}$:

$$\Delta\tau_{bp} = \frac{4\beta\mu b}{\sqrt{\frac{2}{\sqrt{3}\sum_{i>i_c} N_i 2r_i}}} \tag{35}$$

For bypassing of squarely arranged precipitates, CRSS increment due to bypassing becomes:

$$\Delta\tau_{bp} = \frac{2\beta\mu b}{\sqrt{\frac{1}{\sum_{i>i_c} N_i 2r_i}} - \frac{\sum_{i>i_c} N_i l_i}{\sum_{i>i_c} N_i}} \tag{36}$$

With the theoretical limit of $\frac{\sum_{i>i_c} N_i l_i}{\sum_{i>i_c} N_i} < \sqrt{\frac{1}{\sum_{i>i_c} N_i 2r_i}}$.

For the case of plate shape precipitates, the effective intersect radius becomes:

$$\overline{r}_i^* = \sqrt{\frac{\sum_i N_i r_i t_{pi}}{2\sum_i N_i}} \tag{37}$$

And the CRSS increment for the shearing of plate-shaped precipitates becomes:

$$\Delta\tau_{sh} = k^{3/2} \times \frac{1}{2} b_p^2 \sqrt{\frac{\pi \sum_{i<i_c} N_i t_{pi}}{b\beta\mu}} \tag{38}$$

In this case, the critical radius of plates for the triangular distribution to be saturated becomes $\frac{4}{\pi}\sqrt{\frac{\sqrt{3}}{2\sum_i N_i 2r_i}}$. Using Eqs. (10), (20), (21) and (33), the CRSS increment due to bypassing is:

When $\frac{\sum_{i>i_c} N_i r_i}{\sum_{i>i_c} N_i} < \frac{4}{\pi}\sqrt{\frac{\sqrt{3}}{2\sum_i N_{i>i_c} 2r_i}}$:

$$\Delta\tau_{bp} = \frac{2\beta\mu b}{\sqrt{\left(\sqrt{\frac{\sqrt{3}}{2\sum_i N_i 2r_i}} - \frac{\pi}{2}\frac{\sum_i N_i r_i}{\sum_i N_i}\right)^2 + \left(\sqrt{\frac{1}{2\sqrt{3}\sum_i N_i 2r_i}} - \frac{\sum_i N_i t_{pi}}{\sum_i N_i}\right)^2}} \tag{39}$$

When $\frac{\sum_{i>i_c} N_i r_i}{\sum_{i>i_c} N_i} \geq \frac{4}{\pi}\sqrt{\frac{\sqrt{3}}{2\sum_i N_{i>i_c} 2r_i}}$, the CRSS increment is equal to Eq. (35).

For squarely distributed plate-shaped precipitates, the CRSS increment due to bypassing is:

$$\Delta\tau_{bp} = \frac{2\beta\mu b}{\sqrt{\frac{1}{\sum_{i>i_c} N_i 2r_i}} - \frac{\pi}{2}\frac{\sum_{i>i_c} N_i r_i}{\sum_{i>i_c} N_i}} \tag{40}$$

With the theoretical limit of $\frac{\sum_{i>i_c} N_i r_i}{\sum_{i>i_c} N_i} < \frac{4}{\pi}\sqrt{\frac{\sqrt{3}}{2\sum_i N_{i>i_c} 2r_i}}$.

4.3.3. Model parameters

The parameters used to calculate the strength evolution for slip are summarized in Table 2. Shearing of precipitates in Mg-Zn alloy is reported by Wang *et al.* [12] for single crystals with shearing of rod-shaped precipitates with radius ~ 5 nm by basal slip during micropillar compression. This prior micropillar experiment is oriented favourably for basal slip where there is a strong localisation into a shear band. For poly-crystal materials the amount of shear banding is lower as the deformation is disturbed by grain boundaries and multiple slip modes. As a result, precipitate shearing events due to large, concentrated stresses are less likely to occur when the precipitate radius is ~ 5 nm. Therefore, the transition radius r_c between shearing and bypassing in the current study is proposed between 0 to ~ 5 nm, and the value of ~ 2.5 nm is selected as it gives the best fit to represent experimental results, this value is also close to the one proposed by Jain *et al.* [13]. The constant k can be determined using Eq. (11) and the mechanical model for poly-dispersed precipitates coupled with the precipitation model is incorporated into the PreciSo software.

4.3.4. Modelling results of CRSS increment on slip planes

Fig. 8 shows the evolution of CRSS increment on basal plane calculated from the strengthening model when aged at 150 °C and 200 °C. The dominant strengthening effect is the bypassing mechanism of rod-

Table 2
Parameters used for strength model for slip.

Parameters	Value	Reference
β	0.21	[61]
μ (GPa)	17	[47,50]
r_c (nm)	2.5	fitted
k	0.09	Eq. (11)
b (nm)	0.32	[15,62]

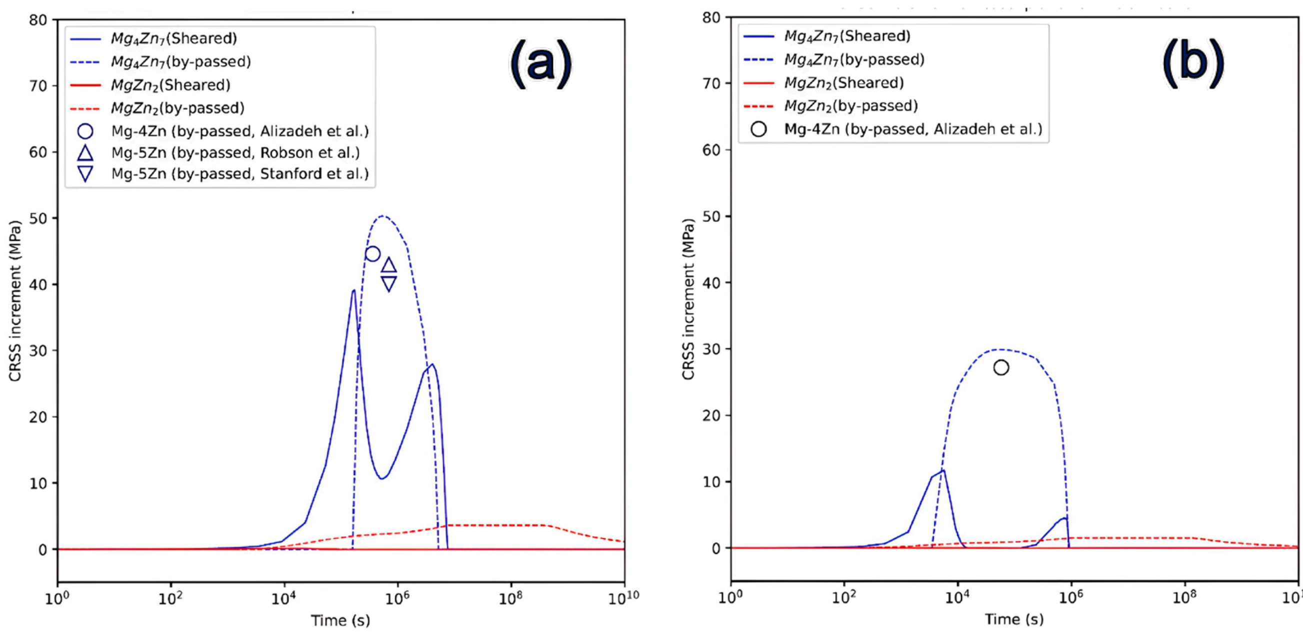

Fig. 8. The kinetics of CRSS increment on the basal plane when aged at (a) 150 °C and (b) 200 °C in Mg-4.5 Zn alloy. Results are compared with the literature [15,63,64], showing that the dominant strengthening effect is the bypassing mechanism of the rod-shaped Mg_4Zn_7 phase, with shearing of rods and bypassing of plate-shaped $MgZn_2$ phase playing roles at early or long aging times.

shaped Mg_4Zn_7 phase, with shearing of rods and bypassing of plate-shaped $MgZn_2$ phase playing roles at early or long aging times. When aged at 150 °C (Fig. 8(a)), shearing dominates hardening initially (peaking at 40 MPa at ~ 27 h), then bypassing takes over as the precipitates grow larger and the peak CRSS increment due to bypassing reaches ~ 50 MPa. When aged at 200 °C (Fig. 8(b)), due to larger precipitate sizes, shearing has only a small initial contribution (up to ~ 3 h) and the bypassing mechanism dominates the strengthening at most aging stages with a peak CRSS increment of ~ 30 MPa. At both temperatures, the peak CRSS increments agree well with Orowan calculations from literature of similar materials and aging conditions [15,63,64]. Notably, this calculation might overestimate the precipitation hardening of basal slip as much lower CRSS increment were reported from experiments (~ 10 – 17 MPa) [12,17]. After peak aging, the CRSS increment from bypassed rod-shaped Mg_4Zn_7 phase starts to drop and is gradually replaced by the bypassing mechanism of plate-shaped $MgZn_2$ phase for longer aging times even though its strength contribution is small.

The evolutions of CRSS increment on prismatic plane evaluated from triangular and square arrangements when aged at 150 °C and 200 °C are presented in Fig. 9. As shown, at both temperatures, shearing of rod-shaped Mg_4Zn_7 phase contributes small CRSS increment in the early aging stages and the strengthening effect from plate-shaped $MgZn_2$ phase is almost negligible. The dominant strengthening mechanism is bypassing of rod-shaped Mg_4Zn_7 phase at all stages. For triangular arrangement, the peak CRSS increments on the prismatic plane at 150 °C and 200 °C are ~ 20 MPa and ~ 10 MPa respectively. Changing to square arrangement will increase the peak CRSS increments of ~ 5 MPa. The results at 150 °C agree with the Orowan calculation from Wang et al. [12] where the CRSS of prismatic slip increased by ~ 20 MPa after peak-aging at 150 °C in a Mg-5 wt.%Zn alloy, but different from some other studies of the same materials and conditions such as Jain et al. [13] (~ 39 MPa), Stanford et al. [11] (~ 70 MPa) and Robson et al. [15] (~ 34 MPa). Despite the different particle arrangements chosen, the scattering results from literature and this study could be due to the influence of various precipitate shape (represented by aspect ratio) observed, this will be discussed in greater details in Section 6.1.

4.4. Model for poly-dispersed precipitates on twinning plane

Based on the results from the precipitation model and strengthening model for slip, several simplifications were made for the twinning model. Firstly, the strength contribution from plate-shaped $\beta_2^{'}$ precipitates is ignored, as they have poor hardening effect (as seen in Fig. 8), due to the large radius and very small number density of precipitates (Fig. 1(a), (b), (c) and (d)). Secondly, the shearing of precipitates by twin dislocations is not considered here since most results in literature [11,12,15,32,38,41] show that the rod precipitates are unlikely to be sheared by twin dislocations.

The principal equation is based on the model proposed by Barnett et al. [47] (Eq. (12)). To calculate $n'b$, L_{twin} and $\overline{D}$ in Eq. (12), the intersect area of rods on the twinning plane is equated to a spherical shape with an effective radius of:

$$\bar{r} = \frac{\sum_i N_i r_i}{\sum_i N_i}\sqrt{\frac{1}{\cos\phi}} \tag{41}$$

Where ϕ is the angle between the $\{10\overline{1}2\}$ twinning plane and the $\{0001\}$ basal plane, calculated using the lattice structural information.

Similar to basal slip, only triangular arrangement is considered here as changing precipitate arrangement does not give significant influence on strengthening prediction. In this case, the area density N_a is:

$$N_a = \frac{2}{\sqrt{3}(L_{twin}+2\bar{r})^2} = \sum_i N_i(2r_i\sin\phi + l_i\cos\phi) \tag{42}$$

Leading to the particle spacing:

$$L_{twin} = \sqrt{\frac{2}{\sqrt{3}\sum_i N_i(2r_i\sin\phi + l_i\cos\phi)}} - \frac{2\sum_i N_i r_i}{\sum_i N_i}\sqrt{\frac{1}{\cos\phi}} \tag{43}$$

With:

$$n'b = b_0'\left(\frac{2\bar{r}}{b}\right)^{\frac{1}{3}} = b_0'\left(\frac{2\sum_i N_i r_i}{b\sum_i N_i}\sqrt{\frac{1}{\cos\phi}}\right)^{\frac{1}{3}} \tag{44}$$

The effective diameter then is:

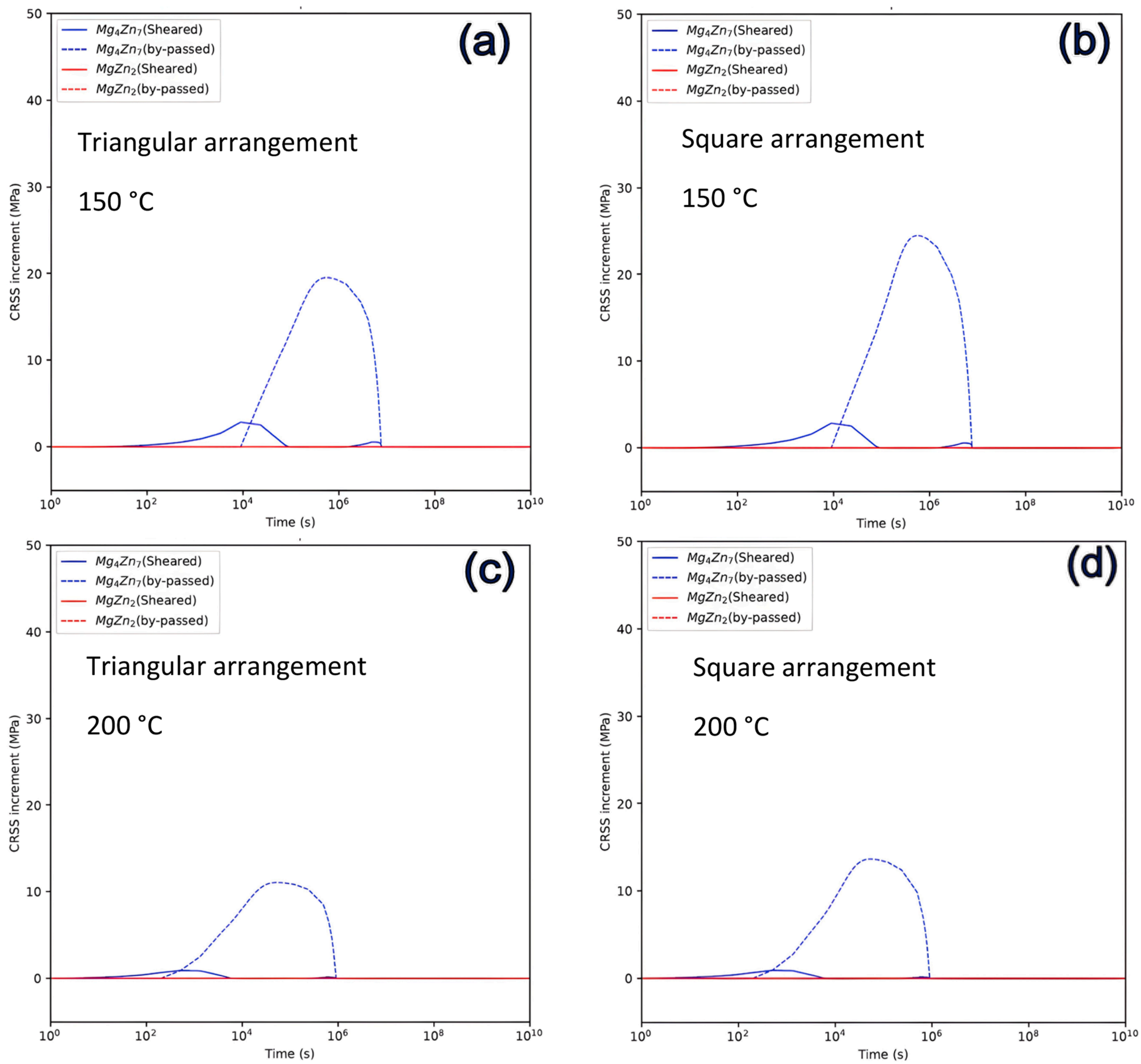

Fig. 9. The kinetics of CRSS increment on prismatic plane evaluated from the triangular arrangement when aged at (a) 150 °C and (c) 200 °C, and evaluated from the square arrangement when aged at (b) 150 °C and (d) 200 °C, in Mg-4.5 Zn alloy.

$$\overline{D} = \frac{2}{\left(\sqrt{\frac{2}{\sqrt{3}\sum_i N_i(2r_i\sin\varnothing + l_i\cos\varnothing)}} - \frac{2\sum_i N_i r_i}{\sum_i N_i}\sqrt{\frac{1}{\cos\phi}}\right)^{-1} + \left(\frac{2\sum_i N_i r_i}{\sum_i N_i}\sqrt{\frac{1}{\cos\phi}}\right)^{-1}} \tag{45}$$

4.4.1. Model parameters

Integrating Eq. (43) - (45) into Eq. (12), the strength increment at each time step can be calculated using the size information of precipitates calculated in Section 3.2. The parameters used for the strengthening model for twinning are shown in Table 3.

Table 3
Parameters used for strengthening model for twinning.

Parameters	Value	Reference
μ (GPa)	17	[47,50]
ν	0.33	[47]
γ (J/m^2)	0.12	[47]
b for twin (nm)	0.049	[47]
τ_0 (MPa)	20	[47]
b'_0 (nm)	0.22	[47]
ϕ (rad)	0.75	This work

4.4.2. Modelling results of CRSS increment on twinning plane

The CRSS increment on twinning plane is calculated by considering the Orowan bypass mechanism of *c*-axis rod-shaped precipitates. The CRSS results, shown in Fig. 10, follow the same kinetics as the rod-shaped precipitates in the precipitation model (Fig. 2). The maximum hardening effects are reached when aging at 150 °C for ~ 84 h or 200 °C for ~ 12 h, the difference in CRSS increment at 150 °C and 200 °C on twinning planes is minor (~ 3 MPa) compared to that on slip planes (a difference of ~ 10 – 20 MPa). It suggests that the hardening effect on slip is more sensitive to the precipitate size variation than that on twinning in the proposed model. This is probably due to the precipitates have better alignment with slip planes than that with twinning planes.

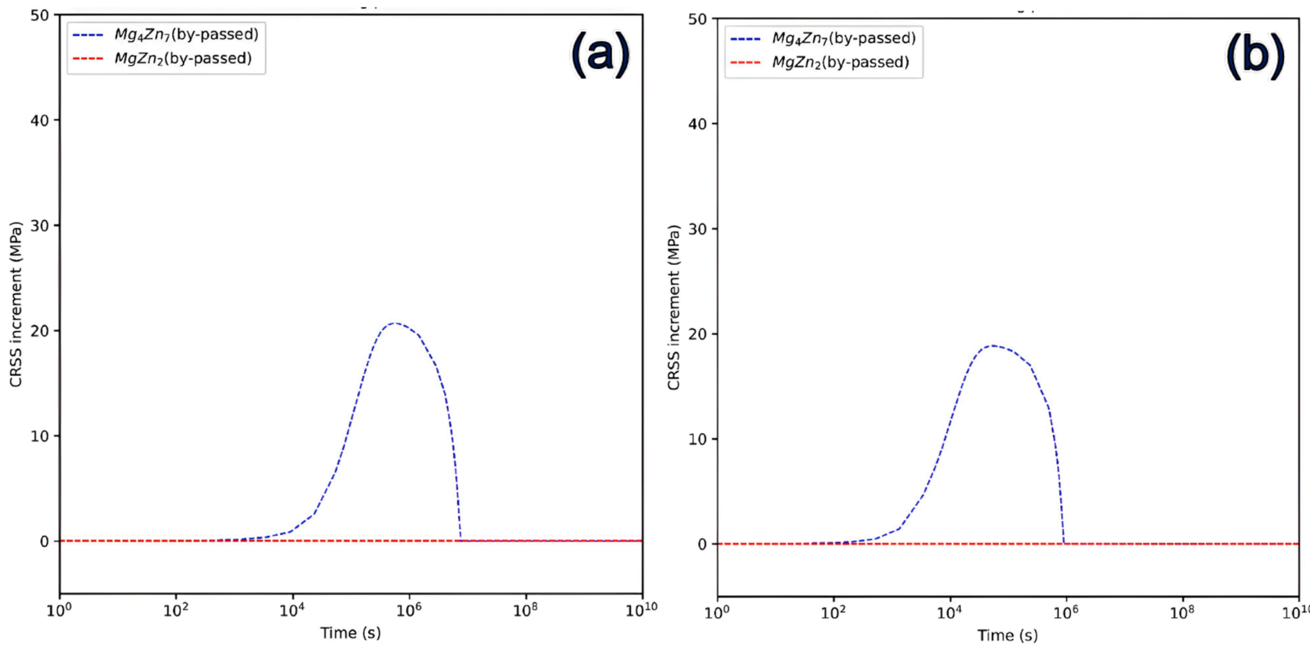

Fig. 10. The kinetics of CRSS increment on twinning plane when aged at (a) 150 °C and (b) 200 °C in Mg-4.5 Zn alloy. The strengthening effect from plate-shaped $MgZn_2$ phase is set to 0.

5. Modelling the yield strength evolution

5.1. Tensile tests along the extrusion direction

To compare the strengthening predictions from the current model and experimental values, several extruded samples with different aging conditions were tested in tension along the extrusion direction. Fig. 11 shows the stress-strain curves of extruded Mg-4.5 Zn alloys aged at different aging conditions. The yield strength increases from ~ 135 MPa in the as-extruded condition to ~ 221 MPa in the peak aged condition at 150 °C. The peak aged yield strength at 200 °C is ~ 206 MPa.

Studies by Agnew *et al.* [65] and Muransky *et al.* [66], using EPSC modelling and in situ neutron diffraction, suggested that while basal slip governs the micro-yielding, the macroscopic yielding is controlled by harder deformation modes. In analytical strength models of Mg alloys [11,13,15], the yield strength is determined by prismatic slip when

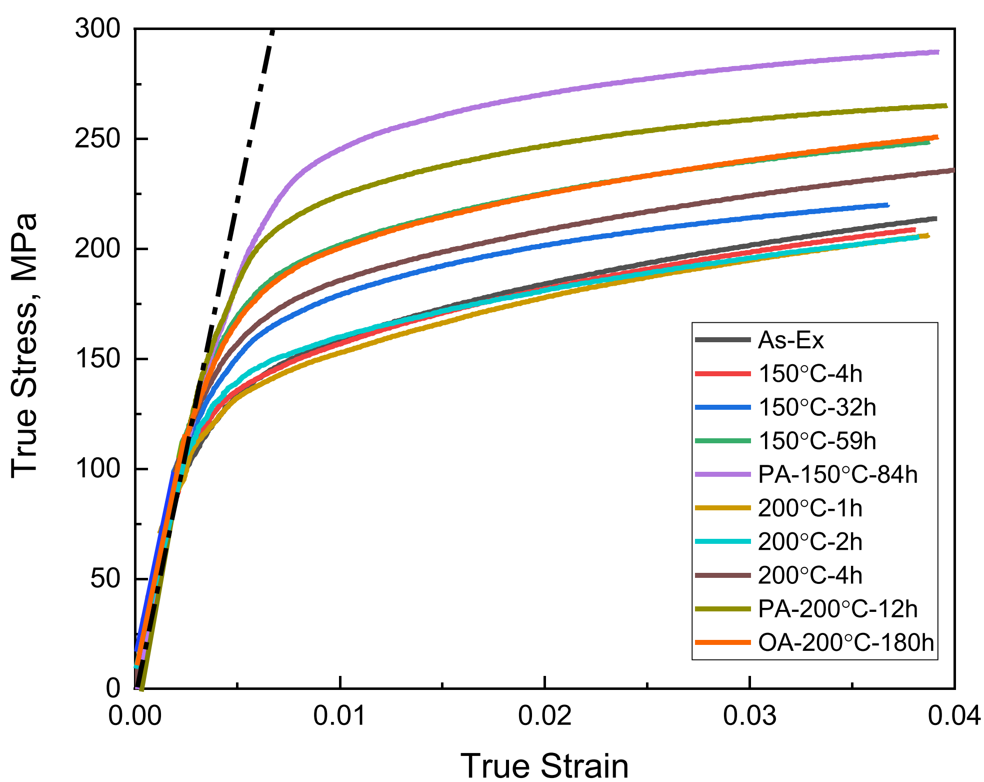

Fig. 11. True stress-strain curves in tension along extrusion direction of Mg-4.5 Zn samples with different aging conditions.

tension is applied along the extrusion direction, and during compression it is controlled by twinning. The calculation of yield strength from the mechanical model is by relating the resolved shear stress $\Delta\tau$ to the macroscopic stress increase $\Delta\sigma$ with the Taylor factor M ($\Delta\sigma = M\Delta\tau$). M is related to the stress-based term $M = \frac{1}{m}$, where m is Schmid factor. For prismatic planes, M was measured as 2.22 from Electron Back Scatter Diffraction (EBSD) maps of the as-extruded material (Appendix Fig. A3 & A4).

The final stress increment is calculated as [53]:

$$\Delta\sigma_{total} = \Delta\sigma_{initial} + \Delta\sigma_{sol} + \Delta\sigma_{p} \tag{46}$$

Where $\Delta\sigma_{initial}$ is the yield strength of the base material, including the contributions from forest dislocations and the Hall-Petch effect which remains constant during aging. $\Delta\sigma_{sol}$ is the solid solution strengthening contribution, expressed as [37,52]:

$$\Delta\sigma_{sol} = k_{Zn}X_{Zn}^{\frac{2}{3}} \ (X_{Zn} \ in \ at.\%) \tag{47}$$

The scaling factor k_{Zn} for Zn can be evaluated from Shi *et al.* [67] and Wang et al. [17] where tensile and compression yield strengths are tested for Mg-Zn alloys with similar grain sizes and different Zn content. The average k_{Zn} for tension and compression are calculated as ~ 10 $\mathrm{MPa}/(at.\%)^{\frac{2}{3}}$ and ~ 11 $\mathrm{MPa}/(at.\%)^{\frac{2}{3}}$, respectively.

The yield strength increment, $\Delta\sigma_p$, from precipitates, considering both shearing and bypassing mechanisms and different precipitate species, is:

$$\Delta\sigma_{(rod\ or\ plate)} = \sqrt{(\sigma_{sh})^2 + (\sigma_{bp})^2} \tag{48}$$

$$\Delta\sigma_{p} = \sqrt{(\sigma_{rod})^2 + (\sigma_{plate})^2} \tag{49}$$

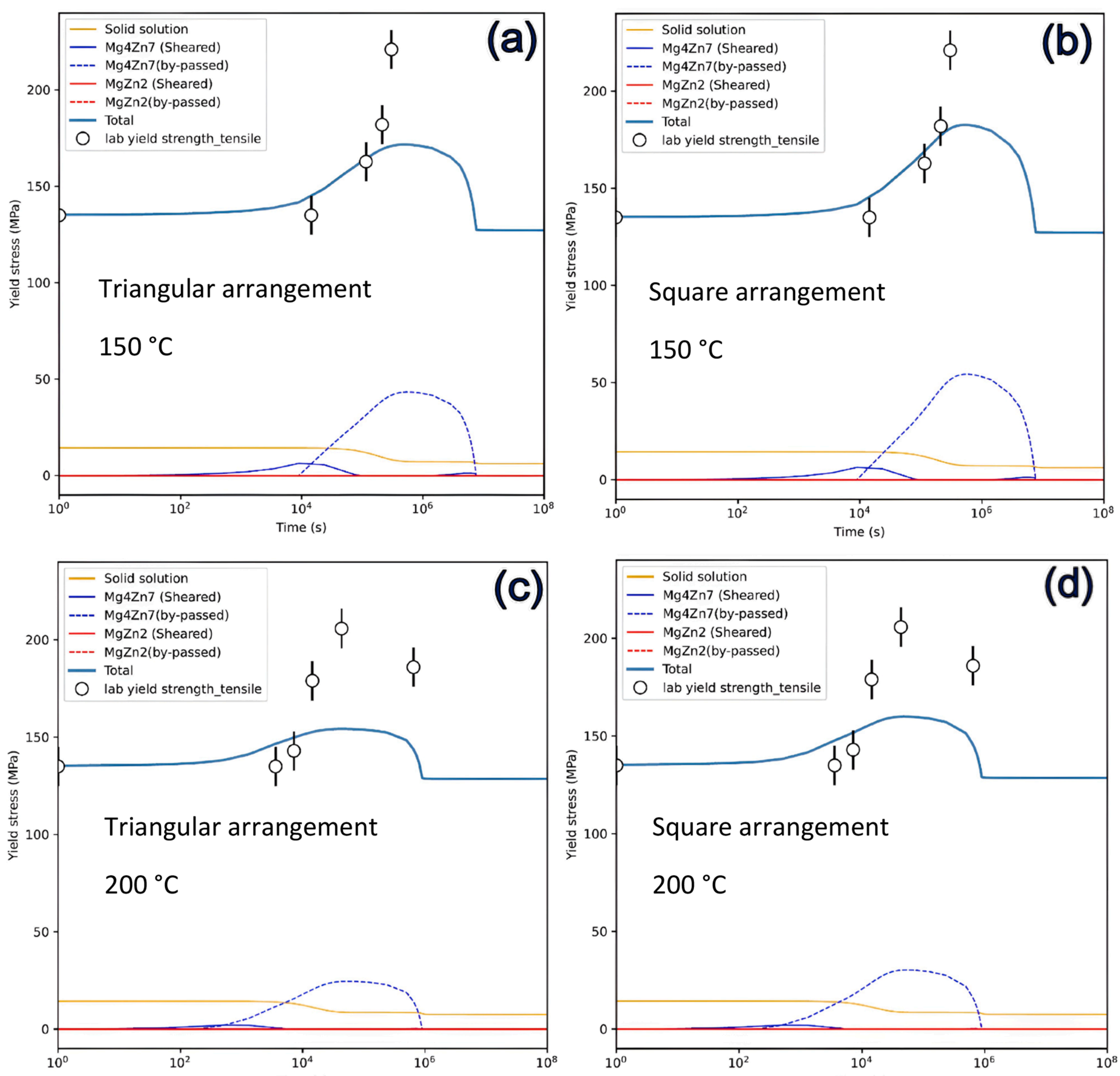

Fig. 12. Comparison between simulated kinetics of yield strength using different particle arrangements and tensile tests results along extrusion direction at (a)(b) 150 °C and (c)(d) 200 °C from Fig. 11. The dominant deformation mechanism is considered as prismatic slip.

The yield strength of the non-aged sample determines the yield strength of the base material with $\Delta\sigma_{initial} + \Delta\sigma_{sol} \approx 135$ MPa. From the initial Zn concentration using Eq. (47), the initial $\Delta\sigma_{sol} \approx 14$ MPa. Therefore $\Delta\sigma_{initial}$ is estimated as ~121 MPa.

The yield strength evolutions for precipitation hardening on prismatic planes calculated from different particle arrangements at 150 °C and 200 °C are compared with experimental results in tension along the extrusion direction in Fig. 12. Note that a global deviation value for experimental results is shown as this is required by the modelling software. This value equals the largest deviation value of all tested conditions (shown in peak-aged samples, ~ 10 MPa) and the same will apply to Fig. 15. It is seen that square arrangement gives slightly higher peak hardening effect that triangular arrangement. At both temperatures, the dominant strength contribution is from the bypassing mechanism of rod-shaped Mg_4Zn_7 phase. The model gives a satisfactory prediction of the yield strength values at early aging stages but underestimates the values around peak aging stage, such underestimation is even higher at 200 °C. This can be due to two things. Firstly, the precipitation model assumes a constant rod aspect ratio, but in reality this parameter is not constant during aging (Yang *et al.* [20]). These deviations could be minor at early aging stage since the shape factor only has limited influence when the overall precipitate size is small, but it becomes more significant when precipitates grow larger. Secondly, the hardening of basal slip could also potentially affect the final yield strength. It is reported that a quarter of the total strain could be attributed by basal slip in this case [66]. The ratio of hardening from the different slip modes is possible to evolve during the precipitation sequence.

5.2. Compression tests along the extrusion direction

Compression tests were conducted for different ageing times at 150 °C and 200 °C. Some representative compressive stress-strain curves of selected conditions are shown in Fig. 13. A yield plateau (or yield elongation) is observed in all conditions. Notably, the length of the yield elongation decreases with ageing time. This is due to the reduced autocatalytic activity of twinning and subsequently lower twin aspect ratio in aged materials [68]. The current result also shows that the yield elongation is inversely proportional to the yield strength in Mg-Zn alloys. Fig. 14 summarizes the yield stresses of all tested conditions. The yield strength increases with aging time in both temperatures and the maximum strength increment (~ 70 MPa) was observed following peak aging at 150 °C. The peak aged strength increment at 200 °C is ~ 40 MPa.

The macroscopic yielding in textured wrought Mg alloys is determined by tensile twinning when compressed perpendicular to the *c*-axis [65]. Using the similar analysis detailed in Section 5.1, the evolution of yield strength during aging can be modelled by considering the precipitation strengthening from twinning. The Taylor factor (inverse of Schmid factor) for twinning measured from Appendix Fig. A3 & A4 is 2.38. Adding it to Eq. (12) and combining with the Eq. (43) - (45), the modelling results can be calculated, as shown in Fig. 15. The simulated yield strength increment agrees well with the experiment results by considering twinning alone, only a slight underestimation around peak aging at 150 °C is shown, with the bypassing of precipitates by twinning dislocations being the dominant mechanism.

6. Discussion

6.1. Precipitation hardening induced by basal and prismatic slip

The current study shows that rod-shaped β_1' precipitates have strong strengthening effect on both basal and prismatic slips.

For basal slip, the rod precipitates are the most effective strengthener since there is a high probability of rod precipitates intersecting the basal plane, and the strengthening effect from precipitates are mainly influenced by the radius according to Eq. (24). The shearing and bypassing mechanisms in the basal plane for rod precipitates in Mg-Zn alloys during aging has been captured and modelled, as shown in Fig. 8. The Orowan bypassing mechanism was found to dominate, agreeing with

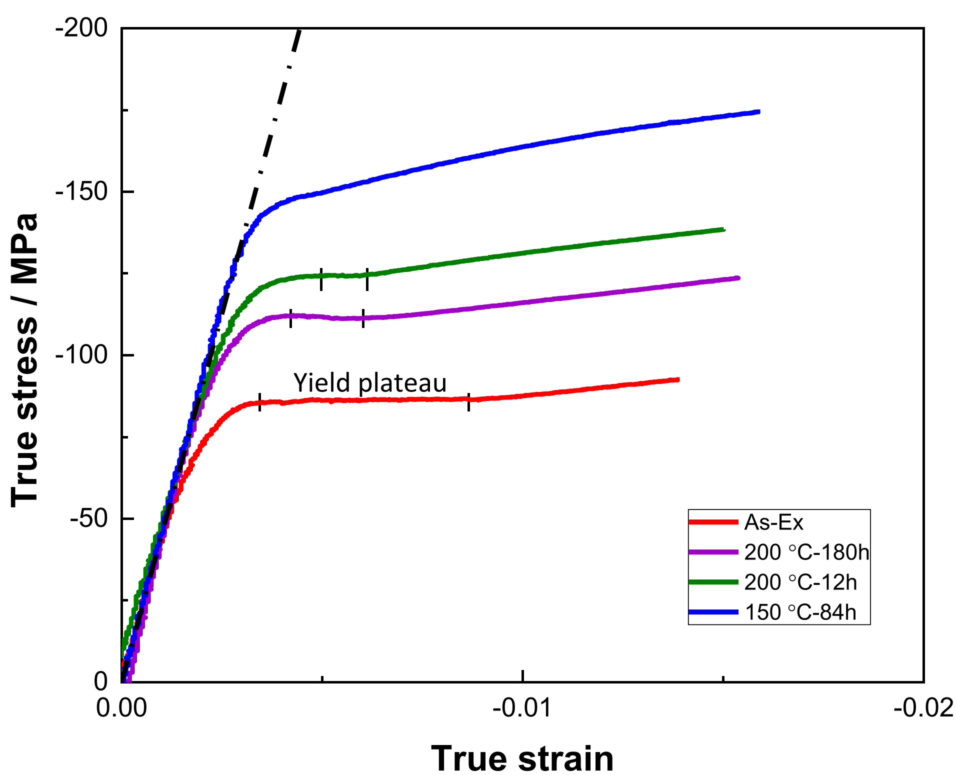

Fig. 13. True stress-strain curves in compression along extrusion direction of Mg-4.5 Zn samples with selected aging conditions. Test was halted at an applied plastic train of 0.012.

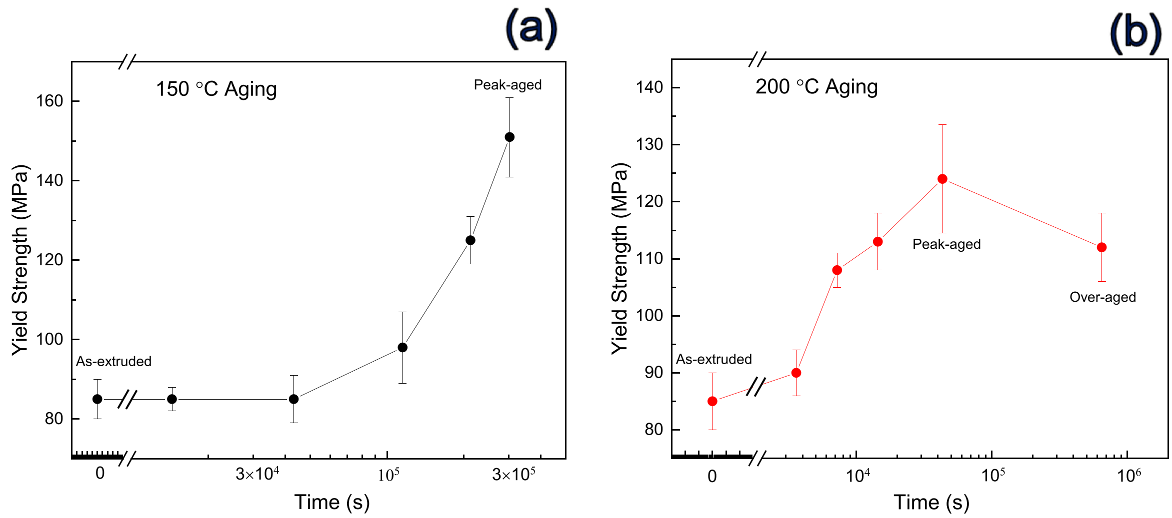

Fig. 14. The 0.2 % yield stress of samples aged at (a) 150 °C and (b) 200 °C, when compressed along the extrusion direction.

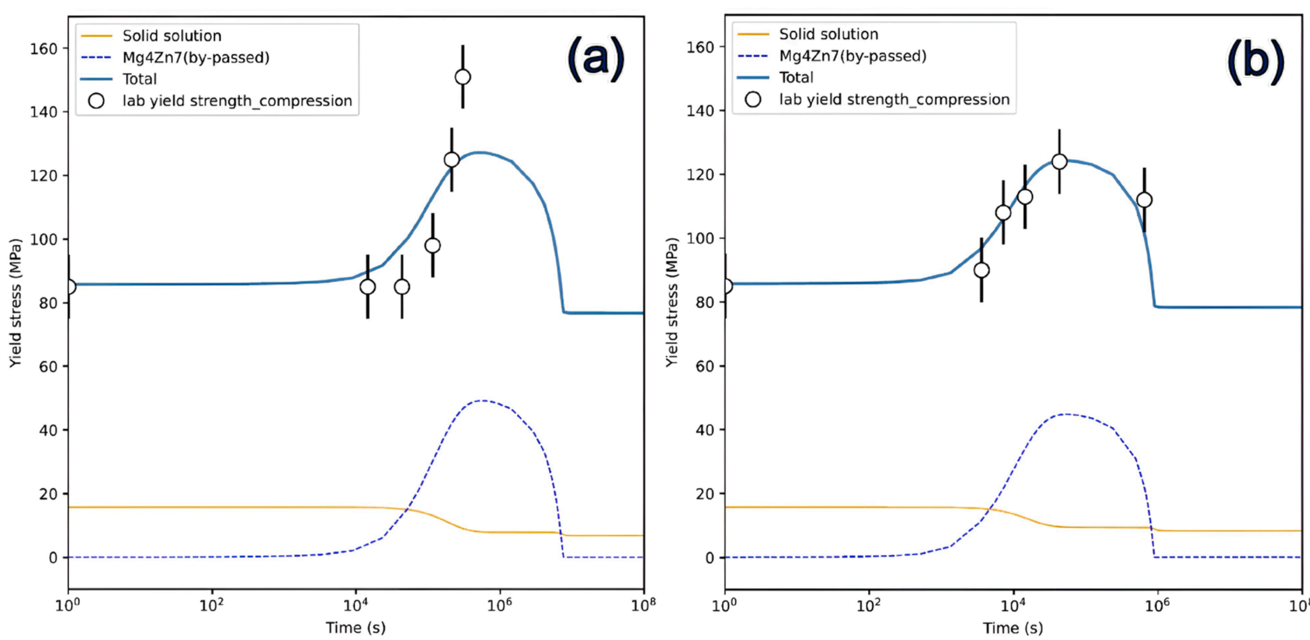

Fig. 15. Comparison between simulated kinetics of yield strength and compression tests results along extrusion direction at (a) 150 °C and (b) 200 °C from Fig. 14. The dominant deformation mechanism is considered as twinning.

prior works [13,15,63,64]. The CRSS increment of basal slip in Mg-Zn alloys after peak-aging at 150 °C or 200 °C is ~ 30 – 50 MPa, which agrees with previous reports from micropillar measurements on single crystals by Alizadeh *et al.* [64]. However, extrapolating these theories to polycrystalline material is still problematic. Wang *et al.* [17] examined CRSS of basal slip in an as-extruded Mg-4.5 Zn alloy before and after peak-aging at 150 °C by testing the onset stress of lattice deviation through XRD, it was found that aging increased the CRSS of basal slip by a mere ~ 10 MPa, a much lower increment than the one from value of Orowan prediction (Fig. 8 and [13,15,63,64]). This discrepancy might be attributed to the limited dislocation source in micropillar sample, accommodating effect of grain boundaries and more activated shear bands in polycrystalline materials.

Shearing of rod precipitates plays a crucial role in precipitation hardening of basal slip especially at early and over-aging stages according to Fig. 8. Wang *et al.* [12] proposed that the shearing of particle is “crystallographically dictated”. In the present case, basal dislocations have an ideal crystallographic matching with a low order plane in rod precipitates, favouring shearing by basal dislocations. Such shearing event has been observed in several studies by TEM in aged Mg-Zn alloys during micropillar tests [12,64,69]. It is suggested that the basal dislocations pile up at the precipitate/matrix interface to accumulate elastic energy before precipitate shearing occurs [69,70], revealing that shearing is controlled by the local elastic energy rather than the precipitate size. Studies have shown that Orowan loops and precipitate shearing coexist in several Mg alloys with large precipitates [64,70-72]. However, shearing in polycrystalline materials might be less observable due to smaller shear on individual slip planes. Additionally, shearing can alter precipitate shapes, affecting subsequent interactions with dislocations [64], an aspect not captured in the model, potentially leading to overestimations.

On the prismatic plane, the strength increment is mostly contributed by the bypassing mechanism, as shown in Fig. 9. Different from basal slip, shearing is less significant for prismatic slip due to the large intersection area of precipitates and less favourable crystallographic match. One consequence is that the equivalent radius of precipitates on the prismatic plane quickly meets the critical value, and the transition from precipitate shearing to precipitate bypassing happens early during aging. In other words, the shearing contribution is capped at a short aging time and limited to small precipitates.

For bypassing mechanism on prismatic plane, the strength increment is very sensitive to the particle shape, as the rod length directly effects the inter-precipitate distance on prismatic planes (Fig. 7). This study used a constant rod aspect ratio of ~ 25, which was taken from the average of overall TEM results in Yang *et al.* [20], to predict the strengthening kinetics due to prismatic slip, this needs to be reconsidered as experiments show that the aspect ratio is changing with aging time and temperature (Table 1 in [20]). One possible reason for this kind of change is related to the varying growth rates of different facets of precipitates. Usually, the incoherent part of the precipitate surface is more mobile [73,74], and the coherent interfacial area is maximized to minimize the overall interfacial energy of the system [75]. In Mg-Zn alloy, both monoclinic Mg_4Zn_7 and hexagonal $MgZn_2$ are proposed as the composition of rod-shaped precipitates [76,77], studies also shown that these two structures can co-exist in the same precipitate [78]. It is, therefore, possible that the rod-shaped precipitates undergo structural transformation during aging, which leads to the variation of interfacial coherency and consequently changing growth rates between facets of precipitates. This is reflected in the current work (Fig. 2(e) and (f)), as aging goes longer, the long rods (with the composition Mg_4Zn_7) are gradually replaced by shorter plates (with the composition $MgZn_2$). Also, the lattice misfit between precipitate and matrix causes elastic stress that can affect particle shape [79]. The changing aspect ratios could be co-influenced by interfacial and elastic energies [80,81].

To illustrate the effect of precipitate aspect ratio, the precipitation hardening effect is plotted against aspect ratios for various conditions in Fig. 16. In this analysis, the precipitate volume fraction and number density are fixed at different values to represent different aging stages for both triangular and square arrangements, while precipitate shape varies with the aspect ratio (from thick and short to thin and long). Several observations can be made: (1) When the precipitate volume fraction and number density are low (corresponding to the early aging stage), the influence of particle shape change on hardening prediction is minor for both particle arrangements, as shown in Fig. 16(a) and (b). In this case, the particle spacing is much larger than the precipitate radius/length and thus, the shape of the particle is insignificant. (2) When the precipitate volume fraction and number density are higher (around the peak aging stage), the hardening calculations become more sensitive to

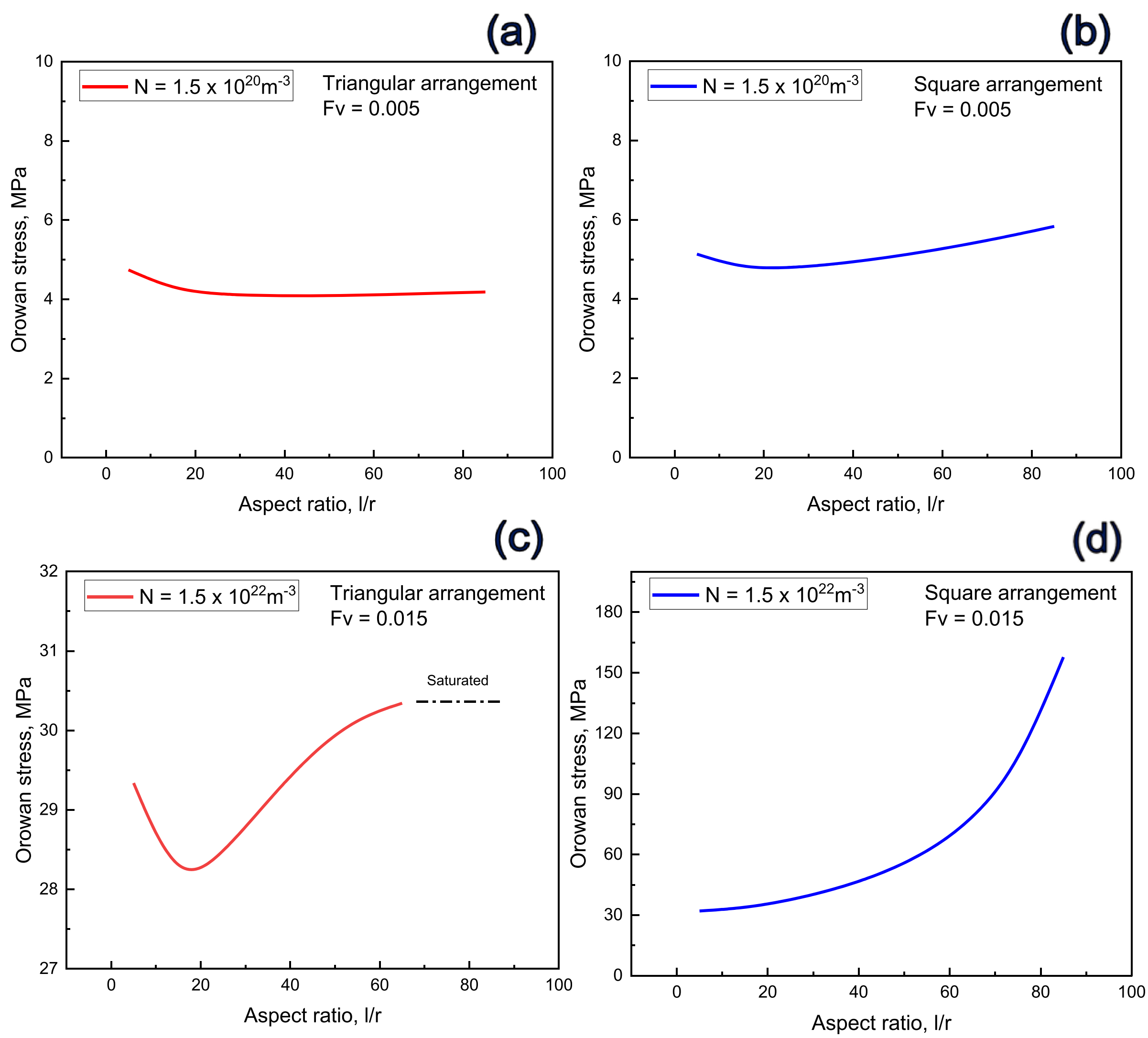

Fig. 16. Influence of precipitate aspect ratio on hardening predictions on the prismatic plane. Tested conditions are estimated from the precipitation model and experimental results in [20], wherein (a) and (b), the precipitate number density (N) and volume fraction (Fv) are fixed at low values to represent early aging stages; in (c) and (d) the precipitate number density and volume fraction (Fv) are fixed at high values to represent peak aging stages.

the particle shape change and easier to meet their theoretical limits (Fig. 7), as shown in Fig. 16(c) and (d). (3) It is also shown that the square arrangement has much faster hardening changes (increased by about five times in the tested range) with aspect ratio compared to the triangular arrangement (<10 %) in Fig. 16(c) and (d). This agrees with the analysis in Fig. 7. It should be noted that there is a drop in hardening prediction with increasing aspect ratio when the aspect ratio is below ~ 20 for triangular arrangement in Fig. 16(c). This means when the precipitate is short, the calculation results from the triangular arrangement are dominated by the precipitate radius, as it decreases when the aspect ratio increases, while when the precipitate is long, the calculation is dominated by the length of precipitate. For the square arrangement, the calculation results are dominated by precipitate length all the time.

Lastly, this study confirms the poor strengthening effect from plate-shaped β_2' precipitates by slip on basal and prismatic planes, as shown in Fig. 8 and Fig. 9, due to their poor alignment and extremely low number densities (Fig. 2(c) and (d)).

6.2. Refining strengthening model for prismatic slip

Our results show that using hardening of prismatic slip for tensile predictions aligns well at early aging stages but underestimates peak aged Mg-Zn alloys' yield strengths (Fig. 12), as also noted in other studies [13]. This is probably due to the lack of consideration of precipitate shape change during aging [20] as discussed in the above section. An improvement strategy is proposed to address this issue by fitting a set of changing aspect ratio into the strengthening model that can satisfy the tensile yield strength at tested conditions. This method has the following assumptions:

- Tensile yield strength along extrusion direction is dominated by prismatic slip [11,13,15].
- Precipitate aspect ratios is increased with aging time before peak aging and decreased with aging time during over aging [20].
- Precipitate aspect ratio is increased with aging temperature [20].

Based on the precipitation size information from the precipitation model (Fig. 2) and the analysis in Fig. 16. A set of aspect ratios are selected and presented in Table 5 that gives best agreement with the lab tested tensile yield strengths, the modeling results are shown in Fig. 17. It can be seen from Table 4 that the fitted aspect ratios are a bit higher than the experimentally observed values [20], this is expected as the precipitation model gives lower predictions of precipitate sizes than the experiment (Fig. 2(a) and (b)).

Table 4
The precipitate aspect ratio that changes with aging conditions to fit the tensile yield strength.

Aging conditions	Fitted aspect ratio (l/r)	Measured aspect ratio from TEM in [20]
Initial value	1	
150 °C - 4h	5	
150 °C - 32h	15	
150 °C - 59h	30	
150 °C - 84 h (peak-aging)	40	~ 29
200 °C - 1h	5	
200 °C - 2h	10	
200 °C - 4h	50	
200 °C - 12 h (peak-aging)	55	~ 37
200 °C - 180 h (over-aging)	15	~ 13

Fig. 17 shows that increasing the aspect ratios of peak aging conditions can significantly improve the model predictions (compared to Fig. 12) at both temperatures. Notably, for short to medium aging time, both particle arrangements lead to close calculation values that agree well with the experimental results. For peak aged conditions, where the shape asymmetry and number density are the highest, there is a bigger discrepancy between square and triangular arrangements, especially at 200 °C. The increased gap between the two estimations over aging time indicates that the strength predictions from both arrangements are getting closer to their theoretical limits (Fig. 7). In this case, the square arrangement tends to overestimate the strengthening effect and the triangular arrangement tends to underestimate, the final value of modelled yield strength is therefore proposed in between the two estimations.

The expressions of aspect ratios for both temperatures are then derived, and could be incorporated into the strengthening model for the current material:

$$\text{For } 150\ ^\circ\text{C}: \ b_r = \left(1.27 \ \times 10^{-4} s^{-1}\right) \times t + 1.76 (\text{before } 84 \ \text{h}) \tag{50}$$

$$\text{For } 200^\circ\text{C}: \ b_r = \left(1.27 \ \times 10^{-3} s^{-1}\right) \times t + 6.78 (\text{before } 12 \ \text{h}) \tag{51}$$

and

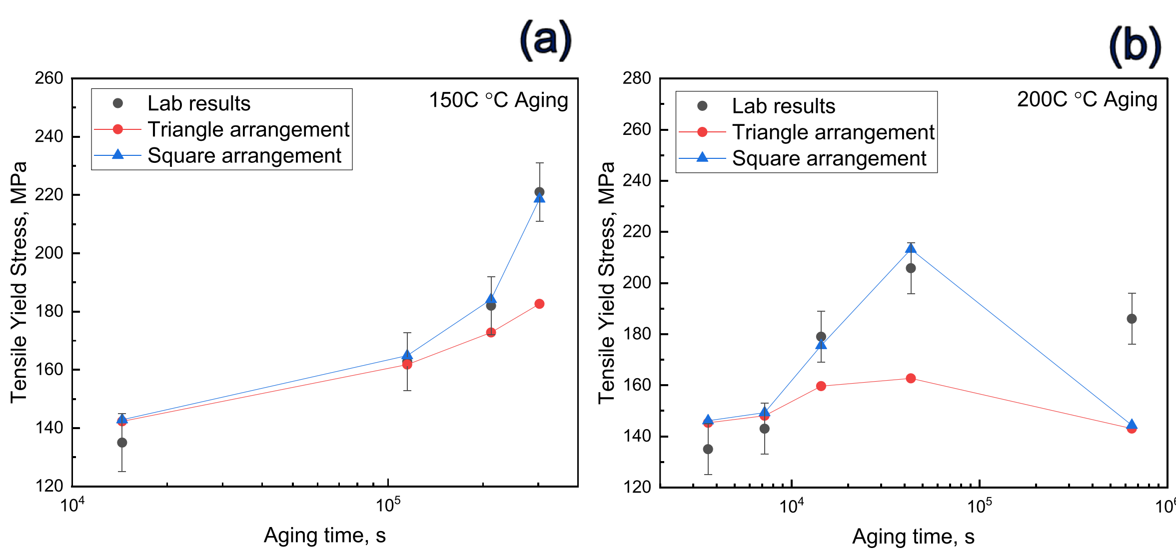

Fig. 17. Modified strengthening model results for prismatic slip with fitted aspect ratio compared with tested tensile yield strength of Mg-4.5 Zn alloys aged at (a) 150 °C and (b) 200 °C.

$$b_r = \left(-6.61 \times 10^{-5} s^{-1}\right) \times t + 57.85 \text{ (after 12 h)} \tag{52}$$

Where b_r is aspect ratio of rod precipitates which can be represented as l/r, t is time with unit s.

Note that this is a rough estimation as the current model does not consider potential contributions from different deformation modes to the final yield strength, and there are still differences between precipitation model and experiments (Fig. 2). Also, the kinetics of precipitate shape change could be influenced by alloy composition and aging temperature. But overall, this work provided a novel reference for modelling the precipitation hardening on prismatic plane in Mg-Zn alloys.

6.3. *Precipitation hardening from twinning*

According to Fig. 15, considering solely the bypass mechanism by twin dislocations gives satisfactory predictions of the strength evolution during aging in Mg-Zn alloys. Precipitate shearing by twin dislocation is less likely given the smaller Burgers vector of twin dislocations compared to slip dislocations and shearing by twinning is rarely observed [11,12,15,32,38,41]. It occurs only in cases with very small precipitates [38-40] and the mechanism to describe these shearing events is still unclear. The unshearable precipitates lead to twin dislocations pile up and subsequent bypass, as proposed by Barnett *et al.* [37]. Studies show [11,15,32,38,41] that the *c*-axis rods are rotated by twinning. This must happen gradually along the rod as the twin front propagates. The local stresses will thus be complex and the uncertainty over their magnitude and variation may account for discrepancies between predictions (CRSS increment of twinning at 150 °C in this study of ~ 20 MPa) compared to the diffraction work of Wang *et al.* [17] (~ 15 MPa).

Also, the current model does not capture several phenomena which may explain the discrepancies between modelling and experimental results, such as:

- The interactions between precipitates and twin boundaries, as interfaces exhibit many different mechanisms that could influence the precipitation hardening effect, compared to dislocations as line defects [82].
- The interactions between precipitates and the back stress and plastic relaxation [83,84].

6.4. *Limitations of the current model*

The strengthening model's results are based on the precipitate size calculated from the precipitation model (ref. [20]) which involves a set of assumptions. Solute effects on CRSS are excluded as it is reported to only have a minor influence [85,86]. Comparisons with polycrystalline materials likely lead to overestimated results due to simplifications like homogeneous precipitate distribution and disregard for structural defects like grain boundaries. In addition, the super dislocation model for twinning does not consider the planar defects that have been reported to form in the twin interfaces [87-89]. Despite these limitations, the current model provides a useful estimate of hardening increments as a function of aging time and temperatures in Mg-Zn alloys.

7. Conclusions

In this paper, the hardening effects of precipitates from slip and twinning in Mg-Zn alloys are investigated through mechanical models coupled with a precipitation model. The main conclusions are summarized as follows:

1. Mechanical models, coupled with a precipitation model, are developed to predict the strength evolution of Mg-Zn alloys during aging. The analysis reveals that rod-shaped β_1' precipitate is the dominant strengthening phase while the plate-shaped β_2' has a minimal strengthening impact.
2. On the basal plane, the shearing mechanism of rod-shaped β_1' precipitates dominates at early aging stages, while the bypassing mechanism becomes gradually more prevalent in medium aging stages.
3. For the prismatic plane, the dominant strengthening mechanism is the bypassing of rod-shaped precipitates. The model effectively estimates yield strength evolution during tensile tests along the extrusion direction, particularly at early aging stages. However, it tends to underestimate the yield stress around peak aging stages; this can be improved by considering changes in the shape factor of the rod-shaped β_1' precipitate.
4. A mechanical model for poly-dispersed precipitates on the twinning plane is developed, providing accurate predictions for strength evolution in compression. This model focuses on the bypass mechanism of rod-shaped precipitates.

Overall, this research advances our understanding of precipitation hardening in Mg-Zn alloys. It highlights the significant role of rod-shaped β_1' precipitates and the limited impact of plate-shaped β_2' precipitates across various aging stages and deformation modes.

CRediT authorship contribution statement

Yi Yang: Writing – review & editing, Writing – original draft, Visualization, Validation, Software, Methodology, Investigation, Formal analysis, Data curation, Conceptualization. **Jun Wang:** Writing – review & editing, Investigation, Data curation. **Mahmoud Reza Ghandehari Ferdowsi:** Investigation, Data curation. **Sitarama R. Kada:** Supervision, Conceptualization. **Thomas Dorin:** Writing – review & editing, Supervision, Methodology, Conceptualization. **Matthew R. Barnett:** Writing – review & editing, Supervision, Resources, Project administration, Methodology, Funding acquisition, Conceptualization. **Michel Perez:** Writing – review & editing, Supervision, Software, Resources, Project administration, Methodology, Investigation, Conceptualization.

Declaration of competing interest

The authors declare that they have no known competing financial interests or personal relationships that could have appeared to influence the work reported in this paper.

Acknowledgements

The authors would like to acknowledge the Deakin Advanced Characterization Facility for supporting the characterization and mechanical testing work. Fundings provided by Australian Research Council Discovery Grant (DP150101577) and China Scholarship Council (201706370176) are highly appreciated.

Appendix

Precipitate strengthening model for slip
Force acting on precipitates

If we consider a dislocation line of Burgers vector b and line vector I, as shown in Fig. A1, located at a region of applied stress contains only yz shear components, and I make an angle α with b, each portion of a dislocation line will be subjected to a stress given by Peach-Koehler force [90]:

$$f = \tau b \times I = \tau b \begin{bmatrix} \sin\alpha \\ \cos\alpha \\ 0 \end{bmatrix} \tag{A1}$$

Where τ is the critical resolved shear stress (CRSS).

The force f will be always perpendicular to the dislocation line and making a circular profile of the dislocation with a radius R. Also, the dislocation is subjected to a line tension $\mathscr{T}$ that is always parallel to the dislocation line. At equilibrium, the net force acting on a dislocation arc length $\mathrm{d}l = Rd\theta = 0$, this gives:

$$\tau bdl = 2\mathscr{T}\mathrm{d}\theta/2 \tag{A2}$$

And therefore:

$$\mathscr{T} = \tau bR \tag{A3}$$

The radius of dislocation line curvature is then inversely proportional to the applied stress. Next, when the dislocation line moves into interaction with particles, the net force acting on neighbouring particles due to the arc of dislocation can be calculated as [53,54]:

$$F = \int_{\alpha_0+\frac{\theta}{2}}^{\alpha_0-\frac{\theta}{2}} \tau b \begin{bmatrix} \sin\alpha \\ \cos\alpha \\ 0 \end{bmatrix} Rd\alpha = 2R\tau b\sin\left(\frac{\theta}{2}\right) \begin{bmatrix} \sin\alpha_0 \\ \cos\alpha_0 \\ 0 \end{bmatrix} \tag{A4}$$

To estimate the net force acting on single particle $\overline{F}_p$, on average we assume the force acting on left and right side of particle are equal:

$$F_{left} = F_{right} = \overline{F}_p/2 \tag{A5}$$

And the distance L between the central particle to its neighbouring particles are equal:

$$L_{left} = L_{right} = L \tag{A6}$$

Noting that:

$$\frac{L}{2} = R\sin(\theta/2) \tag{A7}$$

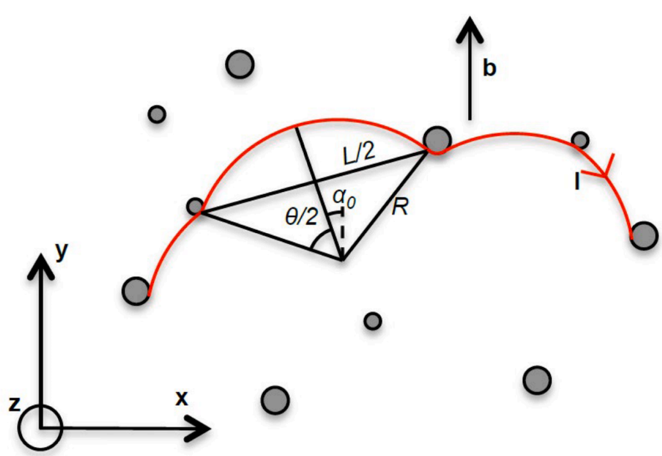

Fig. A1. Dislocation with burger's vector b and line vector I interacting with particles [91].

Finally, we can derive the intensity of the force:

$$\overline{F}_p = \mathrm{L}\tau b \tag{A8}$$

The CRSS increment due to presence of particle is then [53,54]:

$$\Delta\tau_p = \frac{\overline{F}_p}{bL} \tag{A9}$$

Bypassed precipitates

For bypassed precipitates, the dislocation bows until $\theta = \pi$ and $L = 2R$, leading to the force due to bypassed precipitates:

$$F^{bp} = 2\tau bR = 2\mathscr{T} \tag{A10}$$

The line tension $\mathscr{T}$ is often approximated by [37,53,54]:

$$\mathscr{T} = \beta\mu b^2 \tag{A11}$$

Where β is the tension line constant and μ is the shear module.

Then we have:

$$F^{bp} = 2\beta\mu b^2 \tag{A12}$$

Take Eq. (A12) into Eq. (A9), the CRSS increment due to bypassed precipitates is finally:

$$\Delta\tau^{bp} = \frac{2\beta\mu b}{L} \tag{A13}$$

Sheared precipitates

For sheared precipitates, $\overline{F}_p$ can be expressed as [54]:

$$F^{sh} = k\mu b\bar{r} \tag{A14}$$

Where $\bar{r}$ is the average intersect radius of precipitates with the shear plane and k is a constant.

Fig. A2 shows a situation where dislocation line shearing through one particle. The dislocation line swept an area A after shear through an obstacle and before meeting other obstacles (from situation 1 to situation 2, shadow area in Fig. A2). This area contains exactly one obstacle, therefore we have:

$$AN_A = 1 \tag{A15}$$

Where N_A is the area density of precipitates.

The bowing occurs at constant mean critical radius R_c. Since in shearing situation the bowing angles are small, so we can estimate $\sin\theta \approx \theta$, the area A can then be calculated:

$$A = R_c^2\left[\frac{2\theta_c}{2} - \frac{\sin 2\theta_c}{2}\right] - 2R_c^2\left[\frac{\theta_c}{2} - \frac{\sin\theta_c}{2}\right] \approx \frac{R_c^2\theta_c^3}{2} \tag{A16}$$

From Eq. (A7) we know that:

$$L^{sh} = 2R_c \sin(\theta_c / 2) \tag{A17}$$

This leads to:

$$R_c^2\theta_c^3 \approx {L^{sh}}^2\theta_c \tag{A18}$$

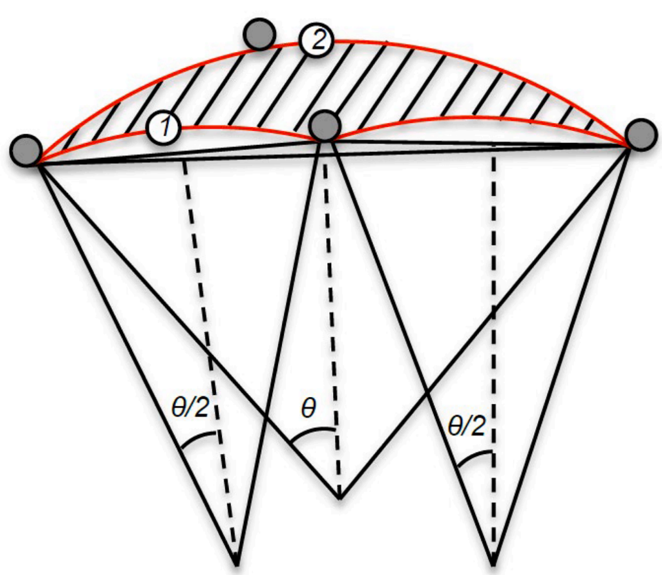

Fig. A2. Dislocation shearing through a particle. The area swept by dislocation line from situation 1 to situation 2 contains one particle [91].

With $AN_A = 1$, we can finally have:

$$\frac{{L^{sh}}^2\theta_c}{2}N_A = {L^{sh}}^2\frac{F^{sh}}{2\mathcal{T}}N_A = 1 \tag{A19}$$

The effective particle spacing is then:

$$L^{sh} = \sqrt{\frac{2\mathcal{T}}{F^{sh}N_a}} \tag{A20}$$

Combine Eq. (A9), (A14) and (A20). The CRSS increment due to sheared precipitates is finally:

$$\Delta\tau^{sh} = \frac{{F^{sh}}^{3/2}}{b}\sqrt{\frac{N_a}{2\mathcal{T}}} = \mu\sqrt{\frac{k^3\overline{r}^3N_a}{2\beta b}} \tag{A21}$$

EBSD measurement for studied material

The EBSD measurement used to evaluate the Schmid factor for basal, prismatic slip and twinning in this study is conducted using a LEO 1530 SEM with the observation plane parallel to the extrusion direction. The step size is 1 μm. Fig. A3 presents the EBSD result for extruded Mg-4.5Zn alloy. Fig. A4 shows the corresponding Schmid factor maps of the basal slip, prismatic slip, and tension twin (when the sample is compressed along ED).

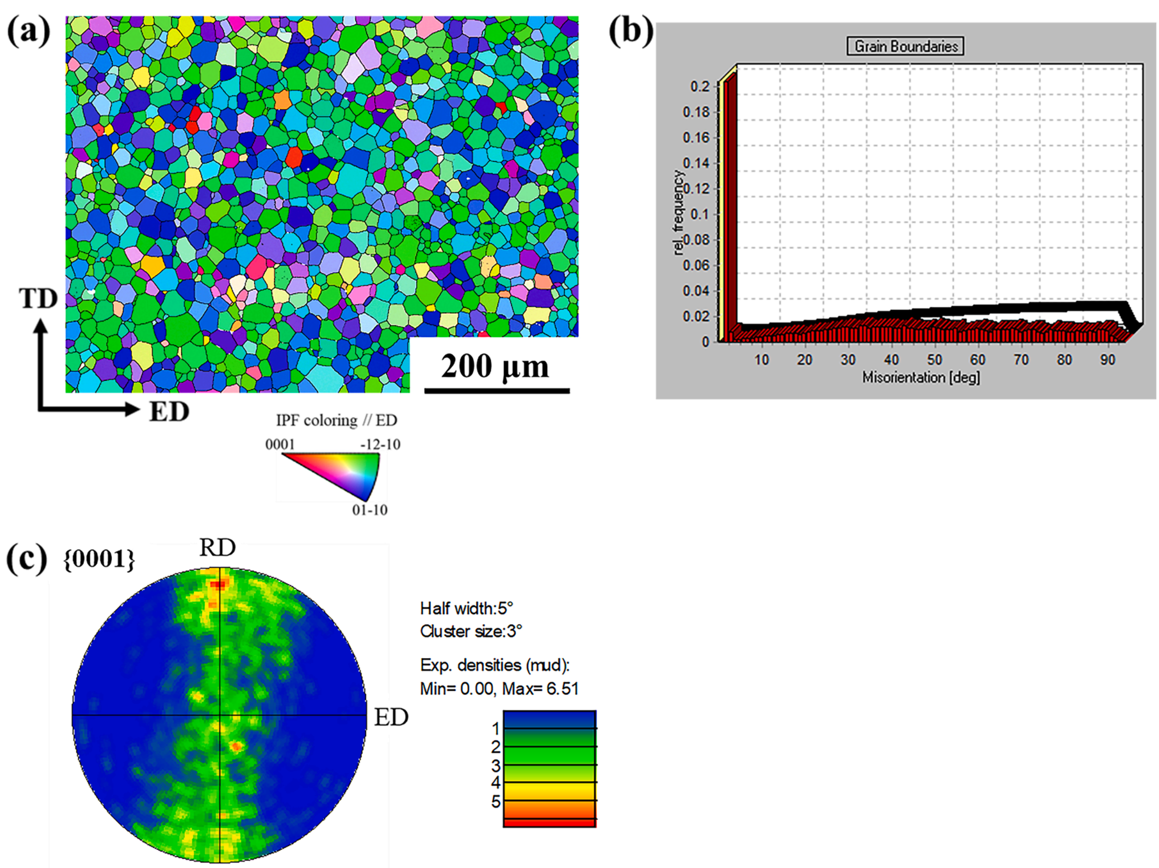

Fig. A3. Microstructures of as-extruded Mg-4.5Zn alloy. (a) is the ED colouring inverse pole figure; (b) is the misorientation plot of (a) showing the absence of peaks corresponding to twinning; (c) is the {0001} pole figure of the as-extruded sample showing a typical extrusion texture with basal plane normal of most grains perpendicular to ED.

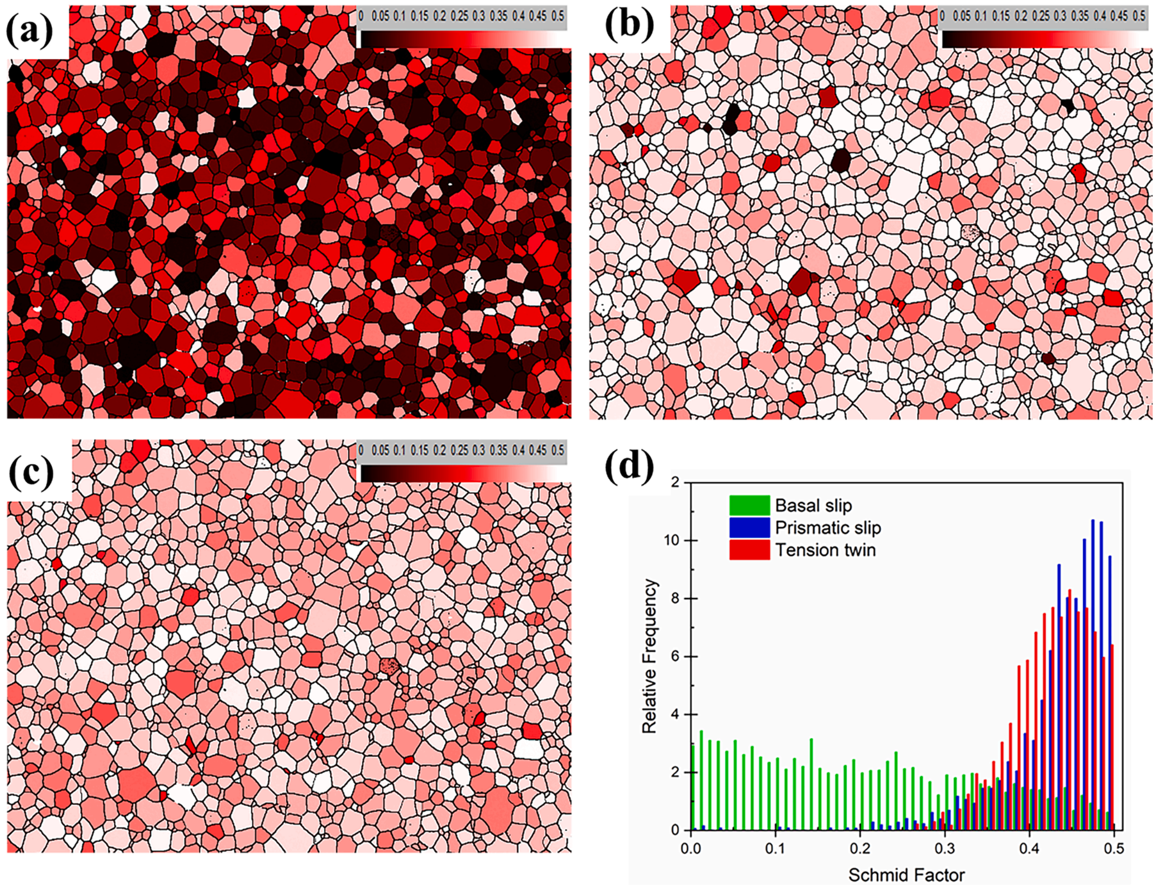

Fig. A4. Schmid factor maps of basal slip (a), prismatic slip (b) and tension twin (c) corresponding to the ED inverse pole figure shown in Fig. A3(a). Their relative frequency comparison is summarized in (d).

References

[1] M. Easton, A. Beer, M. Barnett, C. Davies, G. Dunlop, Y. Durandet, S. Blacket, T. Hilditch, P. Beggs, Magnesium alloy applications in automotive structures, Jom 60 (11) (2008) 57.

[2] J. Hirsch, T. Al-Samman, Superior light metals by texture engineering: optimized aluminum and magnesium alloys for automotive applications, Acta Mater. 61 (3) (2013) 818–843.

[3] W.J. Joost, P.E. Krajewski, Towards magnesium alloys for high-volume automotive applications, Scr. Mater. 128 (2017) 107–112.

[4] S. Zhang, X. Zhang, C. Zhao, J. Li, Y. Song, C. Xie, H. Tao, Y. Zhang, Y. He, Y. Jiang, Y. Bian, Research on an Mg–Zn alloy as a degradable biomaterial, Acta Biomater. 6 (2) (2010) 626–640.

[5] B. Yang, J. Wang, Y. Li, M. Barnett, J. LLorca, Deformation mechanisms of dual-textured Mg-6.5 Zn alloy with limited tension-compression yield asymmetry, Acta Mater. 248 (2023) 118766.

[6] A. Ardell, Precipitation hardening, Metallur. Trans. A 16 (12) (1985) 2131–2165.

[7] J. Clark, L. Zabdyr, Z. Moser, Phase Diagrams of Binary Magnesium Alloys, ASM International, Materials Park, OH, 1988, pp. 353–364.

[8] I. Polmear, Light alloys: from Traditional Alloys to Nanocrystals, Elsevier, 2005.

[9] I. Polmear, Magnesium alloys and applications, Mater. Sci. Technol. 10 (1) (1994) 1–16.

[10] J. Nie, Precipitation and hardening in magnesium alloys, Metallur. Mater. Trans. A 43 (11) (2012) 3891–3939.

[11] N. Stanford, M. Barnett, Effect of particles on the formation of deformation twins in a magnesium-based alloy, Mater. Sci. Eng.: A 516 (1–2) (2009) 226–234.

[12] J. Wang, N. Stanford, Investigation of precipitate hardening of slip and twinning in Mg5% Zn by micropillar compression, Acta Mater. 100 (2015) 53–63.

[13] J. Jain, P. Cizek, W. Poole, M. Barnett, Precipitate characteristics and their effect on the prismatic-slip-dominated deformation behaviour of an Mg–6 Zn alloy, Acta Mater. 61 (11) (2013) 4091–4102.

[14] J. Wang, M.R.G. Ferdowsi, P.A. Lynch, S.R. Kada, M.R. Barnett, Influence of precipitation on tension and compression twinning in Mg-6.5 Zn alloy, Scr. Mater. 207 (2022) 114253.

[15] J.D. Robson, N. Stanford, M.R. Barnett, Effect of precipitate shape on slip and twinning in magnesium alloys, Acta Mater. 59 (5) (2011) 1945–1956.

[16] J.F. Nie, Effects of precipitate shape and orientation on dispersion strengthening in magnesium alloys, Scr. Mater. 48 (8) (2003) 1009–1015.

[17] J. Wang, M.R.G. Ferdowsi, S.R. Kada, P.A. Lynch, Z. Wang, J.A. Kimpton, M. R. Barnett, Stress relaxations during cyclic loading-unloading in precipitation hardened Mg-4.5Zn, Acta Mater. 205 (2021) 116531.

[18] B. Yang, J. Wang, M.R.G. Ferdowsi, Q. Chao, X. Gao, Y. Li, Y. Zhu, M. Barnett, J. Llorca, Effect of precipitates on the dominant active slip systems in Mg-4.5 Zn (wt.%) alloy, Acta Mater. (2024) 120231.

[19] J.M. Rosalie, B.R. Pauw, Form-free size distributions from complementary stereological TEM/SAXS on precipitates in a Mg–Zn alloy, Acta Mater. 66 (2014) 150–162.

[20] Y. Yang, V. Massardier, M.R.G. Ferdowsi, L. Jiang, J. Wang, T. Dorin, S.R. Kada, M. R. Barnett, M. Perez, Revisiting Precipitation kinetics in Mg-Zn alloy – a multi-characterization and modeling study, Acta Mater. 260 (2023) 119276.

[21] E. Kelley, W. Hosford, Plane-strain compression of magnesium and magnesium alloy crystals, Trans. Met. Soc. AIME 242 (1) (1968) 5–13.

[22] Y. Liu, N. Li, M.A. Kumar, S. Pathak, J. Wang, R.J. Mccabe, N.A. Mara, C.N. Tome, Experimentally quantifying critical stresses associated with basal slip and twinning in magnesium using micropillars, Acta Mater. 135 (2017) 411–421.

[23] R. Sánchez-Martín, M.T. Pérez-Prado, J. Segurado, J. Bohlen, I. Gutiérrez-Urrutia, J. Llorca, J.M. Molina-Aldareguia, Measuring the critical resolved shear stresses in Mg alloys by instrumented nanoindentation, Acta Mater. 71 (2014) 283–292.

[24] S. Agnew, C. Tomé, D. Brown, T. Holden, S. Vogel, Study of slip mechanisms in a magnesium alloy by neutron diffraction and modeling, Scr. Mater. 48 (8) (2003) 1003–1008.

[25] S. Agnew, R. Mulay, F. Polesak Iii, C. Calhoun, J. Bhattacharyya, B. Clausen, In situ neutron diffraction and polycrystal plasticity modeling of a Mg–Y–Nd–Zr alloy: effects of precipitation on individual deformation mechanisms, Acta Mater. 61 (10) (2013) 3769–3780.

[26] S.R. Kada, P. Lynch, M. Barnett, *Development of a laboratory-based transmission diffraction technique for* in situ *deformation studies of Mg alloys*, J. Appl. Crystallogr. 48 (2) (2015) 365–376.

[27] H. Abdolvand, M. Majkut, J. Oddershede, J.P. Wright, M.R. Daymond, Study of 3-D stress development in parent and twin pairs of a hexagonal close-packed polycrystal: part I–in-situ three-dimensional synchrotron X-ray diffraction measurement, Acta Mater. 93 (2015) 246–255.

[28] S.R. Kada, P.A. Lynch, J.A. Kimpton, M.R. Barnett, In-situ X-ray diffraction studies of slip and twinning in the presence of precipitates in AZ91 alloy, Acta Mater. 119 (2016) 145–156.
[29] S.R. Agnew, R.P. Mulay, F.J. Polesak, C.A. Calhoun, J.J. Bhattacharyya, B. Clausen, In situ neutron diffraction and polycrystal plasticity modeling of a Mg–Y–Nd–Zr alloy: effects of precipitation on individual deformation mechanisms, Acta Mater. 61 (10) (2013) 3769–3780.
[30] J. Buha, Interrupted Ageing of Al-Mg-Si-Cu Alloys, University of New South Wales, 2005.
[31] Y. Chen, The Effect of Interrupted Ageing on the Strength and Elongation of Precipitation Hardened Aluminium Alloys, Monash University, 2012.
[32] N. Stanford, J. Geng, Y.B. Chun, C.H.J. Davies, J.F. Nie, M.R. Barnett, Effect of plate-shaped particle distributions on the deformation behaviour of magnesium alloy AZ91 in tension and compression, Acta Mater. 60 (1) (2012) 218–228.
[33] E.L.S. Solomon, E.A. Marquis, Deformation behavior of β′ and β‴ precipitates in Mg-RE alloys, Mater. Lett. 216 (2018) 67–69.
[34] J. Wang, N. Stanford, Investigation of precipitate hardening of slip and twinning in Mg5%Zn by micropillar compression, Acta Mater. 100 (2015) 53–63.
[35] J.J. Bhattacharyya, F. Wang, N. Stanford, S.R. Agnew, Slip mode dependency of dislocation shearing and looping of precipitates in Mg alloy WE43, Acta Mater. 146 (2018) 55–62.
[36] T. Nakata, J.J. Bhattacharyya, S.R. Agnew, S. Kamado, Unexpected influence of prismatic plate-shaped precipitates on strengths and yield anisotropy in an extruded Mg-0.3Ca-1.0In-0.1Al-0.2Mn (at.%) alloy, Scr. Mater. 169 (2019) 70–75.
[37] D. Bardel, M. Perez, D. Nelias, A. Deschamps, C.R. Hutchinson, D. Maisonnette, T. Chaise, J. Garnier, F. Bourlier, Coupled precipitation and yield strength modelling for non-isothermal treatments of a 6061 aluminium alloy, Acta Mater. 62 (2014) 129–140.
[38] J. Clark, Transmission electron microscopy study of age hardening in a Mg-5 wt.% Zn alloy, Acta Metallurgica 13 (12) (1965) 1281–1289.
[39] J. Geng, Y. Chun, N. Stanford, C. Davies, J. Nie, M. Barnett, Processing and properties of Mg–6Gd–1Zn–0.6 Zr: part 2. Mechanical properties and particle twin interactions, Mater. Sci. Eng.: A 528 (10–11) (2011) 3659–3665.
[40] M. Matsuda, S. Ii, Y. Kawamura, Y. Ikuhara, M. Nishida, Interaction between long period stacking order phase and deformation twin in rapidly solidified Mg97Zn1Y2 alloy, Mater. Sci. Eng.: A 386 (1–2) (2004) 447–452.
[41] J. Jain, W. Poole, C. Sinclair, M. Gharghouri, Reducing the tension–compression yield asymmetry in a Mg–8Al–0.5 Zn alloy via precipitation, Scr. Mater. 62 (5) (2010) 301–304.
[42] M. Gharghouri, G. Weatherly, J. Embury, The interaction of twins and precipitates in a Mg-7.7 at.% Al alloy, Philos. Mag. A 78 (5) (1998) 1137–1149.
[43] P. Hidalgo-Manrique, J. Robson, M. Pérez-Prado, Precipitation strengthening and reversed yield stress asymmetry in Mg alloys containing rare-earth elements: a quantitative study, Acta Mater. 124 (2017) 456–467.
[44] J. Jain, P. Cizek, W.J. Poole, M.R. Barnett, The role of back stress caused by precipitates on {10-12} twinning in a Mg–6Zn alloy, Mater. Sci. Eng.: A 647 (2015) 66–73.
[45] J. Wang, M. Ramajayam, E. Charrault, N. Stanford, Quantification of precipitate hardening of twin nucleation and growth in Mg and Mg-5Zn using micro-pillar compression, Acta Mater. 163 (2019) 68–77.
[46] N. Stanford, A.S. Taylor, P. Cizek, F. Siska, M. Ramajayam, M.R. Barnett, {10-12} Twinning in magnesium-based lamellar microstructures, Scr. Mater. 67 (7) (2012) 704–707.
[47] M.R. Barnett, H. Wang, T. Guo, An Orowan precipitate strengthening equation for mechanical twinning in Mg, Int. J. Plast. 112 (2019) 108–122.
[48] J.J.M.S. Buha, *E. A,* Reduced temperature (22–100 °C) ageing of an Mg–Zn alloy. 2008. 492(1–2): 11–19.
[49] Q. Tan, A. Atrens, N. Mo, M.-X. Zhang, Oxidation of magnesium alloys at elevated temperatures in air: a review, Corros Sci 112 (2016) 734–759.
[50] A. Balan, M. Perez, T. Chaise, S. Cazottes, D. Bardel, F. Corpace, F. Pichot, A. Deschamps, F. De Geuser, D. Nelias, Precipitation of γ″in Inconel 718 alloy from microstructure to mechanical properties, Materialia (Oxf) 20 (2021) 101187.
[51] M. Perez, M. Dumont, D. Acevedo-Reyes, Implementation of classical nucleation and growth theories for precipitation, Acta Mater. 56 (9) (2008) 2119–2132.
[52] J. Friedel, *Dislocations.(Pergamon Press, Oxford-London-Edinburgh-New York-Paris-Frankfurt*. 1964.
[53] U.F. Kocks, K. UF, A. AS, A. MF, *Thermodynamics and kinetics of slip.* 1975.
[54] A. Deschamps, Y. Brechet, Influence of predeformation and ageing of an Al–Zn–Mg alloy—II. Modeling of precipitation kinetics and yield stress, Acta Mater. 47 (1) (1998) 293–305.
[55] M. Paliwal, I. Jung, Precipitation kinetic model and its applications to Mg alloys, Calphad 64 (2019) 196–204.
[56] J. Robson, C. Paa-Rai, The interaction of grain refinement and ageing in magnesium–zinc–zirconium (ZK) alloys, Acta Mater. 95 (2015) 10–19.
[57] C. Kammerer, N.S. Kulkarni, R.J. Warmack, Y.H. Sohn, Interdiffusion and impurity diffusion in polycrystalline Mg solid solution with Al or Zn, J. Alloys Compound. 617 (2014) 968–974.
[58] K. Momma, F. Izumi, VESTA 3 for three-dimensional visualization of crystal, volumetric and morphology data, J. Appl. Crystallogr. 44 (6) (2011) 1272–1276.
[59] J.M. Rosalie, H. Somekawa, A. Singh, T. Mukai, The effect of size and distribution of rod-shaped precipitates on the strength and ductility of a Mg–Zn alloy, Mater. Sci. Eng.: A 539 (2012) 230–237.
[60] J.F. Nie, B.C.J.J.o.p.e. Muddle, *Microstructural design of high-strength aluminum alloys.* 1998. 19(6): 543–551.
[61] A. Simar, Y. Bréchet, B. De Meester, A. Denquin, C. Gallais, T. Pardoen, Integrated modeling of friction stir welding of 6xxx series Al alloys: process, microstructure and properties, Prog. Mater. Sci. 57 (1) (2012) 95–183.
[62] J.D. Robson, N. Stanford, M.R. Barnett, Effect of precipitate shape and habit on mechanical asymmetry in magnesium alloys, Metallur. Mater. Trans. A 44 (7) (2013) 2984–2995.
[63] N. Stanford, M.R. Barnett, Effect of particles on the formation of deformation twins in a magnesium-based alloy, Mater. Sci. Eng.: A 516 (1) (2009) 226–234.
[64] R. Alizadeh, J. Llorca, Interactions between basal dislocations and β1′ precipitates in Mg–4Zn alloy: mechanisms and strengthening, Acta Mater. 186 (2020) 475–486.
[65] S. Agnew, D. Brown, C. Tomé, *Validating a polycrystal model for the elastoplastic response of magnesium alloy AZ31 using* in situ *neutron diffraction*, Acta Mater. 54 (18) (2006) 4841–4852.
[66] O. Muránsky, D. Carr, M. Barnett, E. Oliver, P. Šittner, Investigation of deformation mechanisms involved in the plasticity of AZ31 Mg alloy: in situ neutron diffraction and EPSC modelling, Mater. Sci. Eng.: A 496 (1–2) (2008) 14–24.
[67] D. Shi, M. Pérez-Prado, C. Cepeda-Jiménez, Effect of solutes on strength and ductility of Mg alloys, Acta Mater. 180 (2019) 218–230.
[68] J. Wang, M.R.G. Ferdowsi, S.R. Kada, C.R. Hutchinson, M.R.J.S.M. Barnett, *Influence of precipitation on yield elongation in Mg-Zn alloys.* 2019. 160: 5–8.
[69] G. Esteban-Manzanares, R. Alizadeh, I. Papadimitriou, D. Dickel, C.D. Barrett, J. Llorca, Atomistic simulations of the interaction of basal dislocations with MgZn2 precipitates in Mg alloys, Mater. Sci. Eng.: A 788 (2020) 139555.
[70] Z. Huang, C. Yang, L. Qi, J.E. Allison, A. Misra, Dislocation pile-ups at β1 precipitate interfaces in Mg-rare earth (RE) alloys, Mater. Sci. Eng.: A 742 (2019) 278–286.
[71] C.M. Cepeda-Jiménez, M. Castillo-Rodríguez, M.T. Pérez-Prado, Origin of the low precipitation hardening in magnesium alloys, Acta Mater. 165 (2019) 164–176.
[72] B. Zhou, L. Wang, G. Zhu, J. Wang, W. Wen, X. Zeng, Understanding the strengthening effect of β1 precipitates in Mg-Nd using In Situ synchrotron X-ray diffraction, JOM 70 (10) (2018) 2315–2320.
[73] C. Sigli, F. De Geuser, A. Deschamps, J. Lépinoux, M. Perez, Recent advances in the metallurgy of aluminum alloys. Part II: age hardening, Comptes Rendus Physique 19 (8) (2018) 688–709.
[74] J. Cahn, G. Kalonji, Symmetry in solid state transformation morphologies, in: Proceedings of an international conference on solidsolid phase transformations, Warrendale (PA), The Metallurgical Society of AIME, 1982.
[75] M.P. Agustianingrum, S.K. Verma, D. Petschke, F. Lotter, T.E. Staab, S. Tang, L. Cao, N. Zulfikar, H. Cho, T.A.J.J.o.A. Listyawan, Compounds, *Revisiting precipitates in Al-Cu-Li alloys: experiments and first-principles calculations of thermodynamic stability of Al2CuLi (T1) precipitate.* 2024. 991: 174495.
[76] X. Gao, J.F. Nie, Characterization of strengthening precipitate phases in a Mg–Zn alloy, Scr. Mater. 56 (8) (2007) 645–648.
[77] L. Wei, G. Dunlop, H. Westengen, Precipitation hardening of Mg-Zn and Mg-Zn-RE alloys, Metallur. Mater. Trans. A 26 (7) (1995) 1705–1716.
[78] J.M. Rosalie, H. Somekawa, A. Singh, T. Mukai, Orientation relationships between icosahedral clusters in hexagonal MgZn2 and monoclinic Mg4Zn7 phases in Mg-Zn (-Y) alloys, Philosophical Magazine 91 (19–21) (2011) 2634–2644.
[79] A. Khachaturyan, Theory of structural transformations in solids Wiley, Transforms, New York, 1983, p. 16.
[80] W. Johnson, P. Voorhees, Elastically-induced precipitate shape transitions in coherent solids. in Solid State Phenomena, Trans Tech Publ, 1992.
[81] A. Khachaturyan, S. Semenovskaya, J. Morris Jr, Theoretical analysis of strain-induced shape changes in cubic precipitates during coarsening, Acta Metallurgica 36 (6) (1988) 1563–1572.
[82] J.W. Christian, S. Mahajan, Deformation twinning, Prog. Mater. Sci. 39 (1) (1995) 1–157.
[83] C. Bettles, M. Barnett, Advances in Wrought Magnesium Alloys: Fundamentals of Processing, Properties and Applications, Elsevier, 2012.
[84] M.R. Barnett, N. Stanford, A. Ghaderi, F. Siska, Plastic relaxation of the internal stress induced by twinning, Acta Mater. 61 (20) (2013) 7859–7867.
[85] N. Stanford, M.R. Barnett, Solute strengthening of prismatic slip, basal slip and {10-12} twinning in Mg and Mg–Zn binary alloys, Int. J. Plast. 47 (2013) 165–181.
[86] A. Tehranchi, B. Yin, W. Curtin, Solute strengthening of basal slip in Mg alloys, Acta Mater. 151 (2018) 56–66.
[87] J. Tu, X.Y. Zhang, Z.M. Zhou, C. Huang, Structural characterization of $\{10\bar{1}2\}$ twin tip in deformed magnesium alloy, Mater. Charact. 110 (2015) 39–43.
[88] B. Xu, L. Capolungo, D. Rodney, On the importance of prismatic/basal interfaces in the growth of (10-12) twins in hexagonal close packed crystals, Scr. Mater. 68 (11) (2013) 901–904.
[89] Q. Zu, X.Z. Tang, S. Xu, Y.F. Guo, Atomistic study of nucleation and migration of the basal/prismatic interfaces in Mg single crystals, Acta Mater. 130 (2017) 310–318.
[90] M. Peach, J. Koehler, The forces exerted on dislocations and the stress fields produced by them, Phys. Rev. 80 (3) (1950) 436.
[91] D. Bardel, A. Balan, G. Meyruey, M. Perez, Y. Yang, *Precipitates strengthening*, in *Internal document.* 2021.